NOTE TO USERS

THE VIABILITY OF CARBON NANOTUBES FOR SPACE-RELATED TECHNOLOGY AND APPLICATIONS

By

Susan P. Song

A THESIS

Submitted to
Michigan State University
in partial fulfillment of the requirements
for the degree of

MASTER OF SCIENCE

Department of Electrical and Computer Engineering

2004

ABSTRACT

VIABILITY OF CARBON NANOTUBES FOR SPACE RELATED TECHNOLOGY AND APPLICATIONS

By

Susan P. Song

Currently there is a critical need to develop non-Si based "radiation-hard" devices and nanotechnology for space applications. A "radiation-hard" device is a device able to withstand a dosage up to 1000 Gray (Gy) before failing. Space technology must be shielded from radiation encountered in space: heavy ions, protons, electrons, and neutrons. Methods for radiation-hardening have included using silicon-on-sapphire [1-5] or silicon-on-insulator substrates, which are however, expensive and fail after a period of time. Silicon-based devices fail due to destruction of p-n junctions. Carbon nanotube (CNT) based technology is not based on conventional p-n junctions with charge-separated regions. CNT-based space technology could also bring the advantages of cost and size reduction. At the time of this writing, only a few papers, which are theoretical [6-7], have been published on the potential effect of radiation on CNTs. However, to the best of this author's knowledge, the experiments outlined in this thesis are the first such experiments in which the effect of radiation on the properties of CNTs has been investigated in such a well calibrated experiment.

This work is dedicated to my family and friends for all their love and support, to my major professor Dr. Virginia Ayres, for her wonderful patience, guidance and support, and to God, the maker of all creation and to those around me who helped in all the "little ways"

ACKNOWLEDGEMENTS

I would like to thank Dr. Barbara O'Kelly, Dr. Percy Pierre and Mrs. Linda Leon, for their guidance and support during both my undergraduate and Master's program; Dr. Donnie Reinhard, Dr. Timothy Grotjohn and Dr. Timothy Hogan for their guidance and support; Mr. Ben Jacobs, Dr. Reginald Ronningen and Dr. Albert Zeller for their generous time and effort with the radiation portion of the project; The staff of the ECE department: Mrs. Joyce Foley, Mrs. Sheryl Hulet, Mrs. Vanessa Mitchner, Ms. Marilyn Shriver, Ms. Pauline Vandyke and Mrs. Margaret Conner, for their support; Dr. Corey Collard, Dr. Mary Brake and Dr. John Holloway for their tremendous time and effort into growth portion for this project; Dr. Ronald Gilgenbach for the use of the GEC cell at the University of Michigan; Dr. Martin Crimp for training me on the use of his TEM and SEM, and for analyzing the TEM and SEM images; Dr. Ben Simkin, Mr. Steve Ng, Dr. Krishna Boyapati and Dr. Liang Zeng, for their additional guidance on the SEM and TEM; Mr. John Heckman for the HR-TEM images of University of Michigan samples and guiding me with TEM sample preparation techniques; Dr. Melvin Schindler for providing the electrospun carbon nanofibers. The staff of the ChEMS Department, especially Mrs. Nancy Albright and Mrs. JoAnn Peterson, for their wonderful support; Dr. Xudong Fan for the HR-TEM images of the NASA Goddard Space Flight Center CNTs and University of Michigan samples; Ms. Shavesha Anderson, for showing me how to weld CNTs; Dr. Jeannette Benavides, Mr. Harry Shaw and Dr. Jeannette Plante for their guidance and support; NASA and United Negro College Fund Special Programs Corporation for their financial support, without which, I would not have been able to pursue my degree; Dr. Kendrick Curry, for his encouragement and moral support.

TABLE OF CONTENTS

LIST OF FIGURES

LIST OF TABLES

INTRODUCTION

This work described in this thesis investigates the effect of space radiation, specifically at low-earth orbit (LEO), on the properties of carbon nanotubes (CNTs) in order to determine their viability for space applications. LEO is the region ranging from 10 km to 1000 km above the earth. Potential space applications of carbon nanotubes include: self-repairing materials for the skins of shuttles or space suits, new space-resilient electronics, flat-panel displays and even space elevators.

Heavy ions are a significant source of radiation and are encountered in LEO at high declination. The heavy-ion, and trapped particle regions are illustrated in Figure 1. Current transistor-based electronics technology requires radiation shielding against heavy ions, which are massive, charged particles. The amount of shielding required for effective defense against heavy ions would be mass-prohibitive. Radiation effects are classified into non-destructive errors, which can be overcome by device reset and destructive errors, which cause permanent device malfunction. Examples of radiation effects include: Single Event Upset (SEU), a change of state or transient induced by an ionizing particle such as a cosmic ray or proton in a device; Single Event Functional interrupt (SEFI)/Single Event Transient (SET), a condition where the device stops operating in its normal mode, and usually requires a power reset or other special sequence to resume normal operations; Single Hard Error (SHE), an SEU which causes a permanent change to the operation of a device; Single Event Latchup (SEL), a potentially destructive condition involving parasitic circuit elements forming a silicon controlled rectifier (SCR); Single Event Gate Rupture (SEGR), the burnout of a gate

insulator in a power MOSFET and a destructive condition; Lastly, Single Event Burnout (SEB) which is a highly localized burnout of the drain-source in power MOSFETs, which is also a destructive condition. All the previously mentioned damage mechanisms are serious problems for current transistor-based electronics in space applications.

Since their discovery over a decade ago by Iijima [8], CNTs have spawned a wave of research into their potential applications. NASA is particularly interested in the development of CNT-based electronics and textiles which are space-qualifiable. Investigations into the potential use of CNTs as cold cathode sources have also been conducted [9-11].

CNTs are essentially self-closed sheets of graphite. CNTs are either single-wall or multi-wall. Single-wall CNTs can be either separate or bundled in a rope containing twenty to fifty individual nanotubes in a triangular lattice (hexagonal close-packed stacking); the latter is shown in Figure 2 (a)-(b). Individual single-wall CNTs are generally on the order of 0.7-2 nm in diameter and several microns in length. The mean diameters of single-wall CNTs (both individual and bundled), and the inter-tube distances for bundled CNTs, are dependent on the catalyst used and the growth conditions. Individual, separate single-wall CNTs, to best of this author's knowledge, have been synthesized only in the presence of any one of the transition metals such as iron, nickel, copper or cobalt or lanthanides, such as lanthanum, yttrium, gadolinium and neodymium.

Multi-wall CNTs consist of several layers, with the diameter of the outermost wall ranging from 20 to 30 nm, are also generally up to several microns in length. An example of a multi-wall CNT of about 15 layers is shown in Figure 3. Various unique forms, curly or Y-junction, of CNTs have been reported as well [12].

In the course of the research presented in this thesis, first time studies of heavy ion interaction in carbon nanotubes and other new nanoscale materials have been conducted. Our results show high radiation resilience for single and multi-wall CNTs, which indicate that carbon nanotubes may have good potential for space applications.

The organization of the thesis is as follows: In Chapter 1, we review the basic properties of CNTs. In Chapter 2, the main experimental techniques used in the research are described. In Chapter 3, synthesis of the carbon nanotubes investigated in this thesis is discussed. The synthesis research included system components at Michigan State University, at the University of Michigan, and at the NASA Goddard Space Flight Center. Parts of the research were done in collaboration with these two institutions. The heavy ion radiation experiments and their results are described in Chapter 5. Our conclusions are discussed in Chapter 6.

CHAPTER 1
PHYSICAL STRUCTURE AND IDEAL ELECTRONIC AND MECHANICAL PROPERTIES OF CARBON NANOTUBES

Ideal properties of carbon nanotubes (CNTs), for better understanding of their applications potential, and also for understanding of what a radiation-induced deviation from ideal would entail, are described in this Chapter. Theoretical growth mechanisms are briefly discussed, since part of the research presented in this thesis involved the growth of multi-wall carbon nanotubes and nanotube-nanowire heterostructures.

An excellent reference for theoretical and some experimental properties of carbon nanotubes is "Physical Properties of Carbon Nanotubes", by R. Saito, G. Dresselhaus, and M.S. Dresselhaus, published by Imperial College Press (1998). This reference is extensively quoted in this section.

Physical structure of a single-wall CNT

A single-wall CNT is a single-layer seamless cylindrical graphene tube. There are three key vectors that define the structure of a single-wall CNT: the chiral (which also defines the "handedness" of a CNT, *i.e.*, whether the nanotube is "rolled" clockwise or counter-clockwise), translational and symmetry vectors. These vectors are shown in Figure 4.

The chiral vector is denoted as $\overline{C_h}$, and is represented by $\overline{OA}$ in Figure 3. The vector $\overline{OA}$ is a unit vector in the direction perpendicular to the nanotube axis, or equator, of the

nanotube and $\overline{OB}$ is in the direction of the nanotube axis. $\overline{T}$, the translational vector, is a unit vector in the direction of $\overline{OB}$ in the Figure, and $\overline{R}$, in the direction of $\overline{OR}$ in Figure 4, is the symmetry vector. The chiral vector, $\overline{C_h}$ is defined by

$$\overline{C_h} = n\overline{a_1} + m\overline{a_2} \equiv (n,m) \qquad (1)$$

where n and m are integers, $\overline{a_1}$ and $\overline{a_2}$ are the unit vectors in real space of the CNT, and $0 \leq |m| \leq n$.

The unit cell of a single-wall CNT is given by rectangle formed by the translation vector, $\overline{T}$ and the chiral vector, $\overline{C_h}$ shown in Figure 4. Single-wall CNTs can be chiral (non-symmorphic) or achiral (symmorphic). Achiral single-wall CNTs, have a mirror plane, whereas chiral or non-symmorphic, nanotubes have no mirror plane. There are two types of achiral single-wall nanotubes: armchair and zigzag (Figure 4). The names armchair and zigzag are derived from the shape of the cross-section formed when a nanotube is "cut" along its equator. Each of the end caps of the CNTs contains six pentagons and an appropriate number and location of hexagons. Additionally, the armchair nanotube corresponds to the condition when n=m, *i.e.*, when $\overline{C_h}$ = (n,n) and the zigzag nanotube corresponds to the case when m=0, or $\overline{C_h}$ =(n,0). All other (n,m) chiral vectors correspond to chiral nanotubes.

The chiral angle, θ, determines the angle at which the graphitic sheet is "rolled up" to make the CNT. It is defined by the following relationship:

$$\cos\theta = \frac{\overline{C_h} \bullet \overline{a_1}}{\left|\overline{C_h}\right|\left|\overline{a_1}\right|} \qquad (2)$$

The diameter of a single-wall CNT, d_t, is given by

$$d_t = \frac{L}{\pi}, \text{ where } L = \left|\overline{C_h}\right| = \sqrt{\overline{C_h} \bullet \overline{C_h}} = a\sqrt{n^2 + m^2 + nm} \tag{3}$$

where n and m are the indices of the CNT, L is the length of the nanotube and $\overline{a_1} \cdot \overline{a_1} = \overline{a_2} \cdot \overline{a_2} = a^2$. For the CNT, a=.144 nm.

The translational vector is defined to be the unit vector of a 1D CNT and is parallel to the nanotube axis. The translational vector is defined by:

$$\overline{T} = \overline{t_1 a_1} + \overline{t_2 a_2} \equiv (t_1, t_2), \text{ where } t_1 \text{ and } t_2 \text{ are integers} \tag{4}$$

Finally, the symmetry vector $\overline{R}$ is described by the following,

$$\overline{R} = p\overline{a_1} + p\overline{a_2} \equiv (p, q) \tag{5}$$

where p and q are integers and do not have a common divisor except unity. The symmetry vector $\overline{R}$ is defined as the site vector having the smallest component in the direction of $\overline{C_h}$.

The brillouin zone of a single-wall CNT is the same as the brillouin zone of the single graphene sheet. It is defined by two unit vectors b_1 and b_2, where

$$b_1 = \frac{2\pi}{a} * (\frac{1}{\sqrt{3}} x + y), \quad b_2 = \frac{2\pi}{a} (\frac{1}{\sqrt{3}} x - y)$$

and a=$\sqrt{3}$ * the bond length between carbon atoms. This is a standard derivation of the reciprocal space unit vectors b_1 and b_2 from the real space unit vectors.

$$a_1 = a * (\frac{\sqrt{3}}{2} x + \frac{1}{2} y), \quad a_2 = a(\frac{\sqrt{3}}{2} x - \frac{1}{2} y)$$

and

$$\overline{a_i} \bullet \overline{b_j} \equiv 2\pi\delta_{ij}$$

but it is implemented within the appropriate 2 – D space. The real and reciprocal space unit vectors are shown in Figure 6 (a)-6 (b).

Physical structure of a Multi-wall CNT

Multi-wall CNTs are usually formed by ten to twelve concentric graphene layers. In general, each of the individual concentric layers will keep their respective electronic properties and not be commensurate, *i.e.*, the carbon atoms of each of the comprising nanotubes will not be aligned with each other. The interlayer spacing is slightly less than that of graphite, being 0.34 nm.

Electronic properties of Single-wall CNTs

The diameter and chirality of single-wall CNTs determine whether they are metallic or semi-conducting. Two-thirds of all CNTs are semi-conducting, while the other third are metallic [13]. Semi-conducting CNTs have a band gap between of about 1 eV. More specifically, the arm-chair nanotubes, denoted by (n,n) are always metallic and the zigzag nanotubes, denoted by (n,0) are metallic when n is a multiple of 3, semi-conducting otherwise. This results in two categories for metallic CNTs. Metallic zigzag CNTs are all in the metal-1 category. The arm-chair single-wall CNTs are in the metal-2 category. Figure 6 shows the indices of the CNTs in relation to their conductivity and illustrates how the indices are determined.

The relationship between the diameter and chirality of single-wall CNTs and their electronic properties is as follows. $\overline{K_1}$ is the reciprocal lattice vector in the direction of the chiral vector, $\overline{C_h}$, of a single-wall CNT. The condition for metallic energy bands is that the ratio of the length vector $\overline{YK}$ to that of $\overline{K_1}$ is an integer. $\overline{YK} = (2n+m)/3 \times \overline{K_1}$, where n and m are integers that represent the number of carbon atoms in the same corresponding positions in the hexagonal rings of carbon which are crossed horizontally and downwards, respectively, to form the chiral vector on the honeycomb-like lattice of an unrolled CNT. The wave vectors are shown in Figure 6 (c).

Another important property of CNTs (both multi-wall and single-wall) is ballistic or quasi-ballistic transport. Ballistic transport refers to single electron or quantum transport, in which there is no scattering of electrons in the nanotube. Mathematically the quantum conductance, G_0, can be expressed as

$$G_0 = \frac{2e^2}{h} \tag{6}$$

where e is the charge of an electron and h is Planck's constant, and the factor of two in the expression comes from the fact that single wall nanotubes have two conducting channels. Ballistic transport represents the special case when $L << L_\psi << L_m$, where L is the length of the wire, L_m is the momentum relaxation length and L_ψ is the phase relaxation length. Momentum relaxation refers to the average distance that an electron wave function travels in a conductor or semiconductor before its momentum is

randomized due to a collision, and phase relaxation refers to the average distance that an electron wave travels in a conductor or semi-conductor before its phase is randomized due to scattering. In other words, nanotubes exhibit ballistic transport because of their extremely small size, and in ballistic transport there is little or no scattering which results in very high current flow.

Semiconducting CNTs have been successfully doped p-type and n-type. Hence, diodes, which are a junction between p and n-type semiconductors, have been developed using crossed CNTs [14]. However, the role of the p-n doping versus the effect of the contacts in affecting the diode action is currently under investigation.

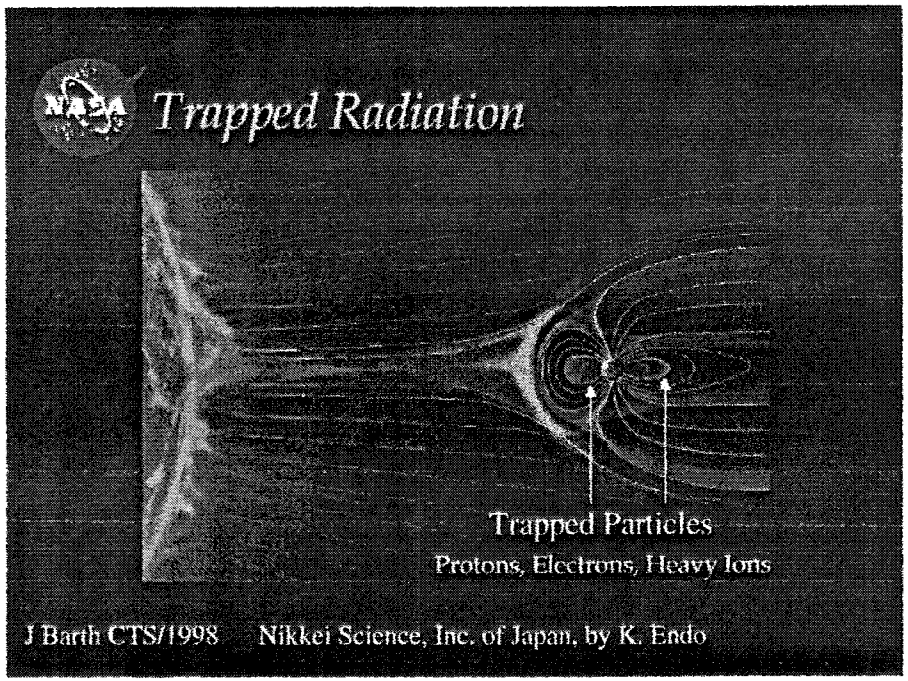

Figure 1a: Regions Where Heavy-Ion and Other Forms of Radiation are encountered in Low-Earth Orbit

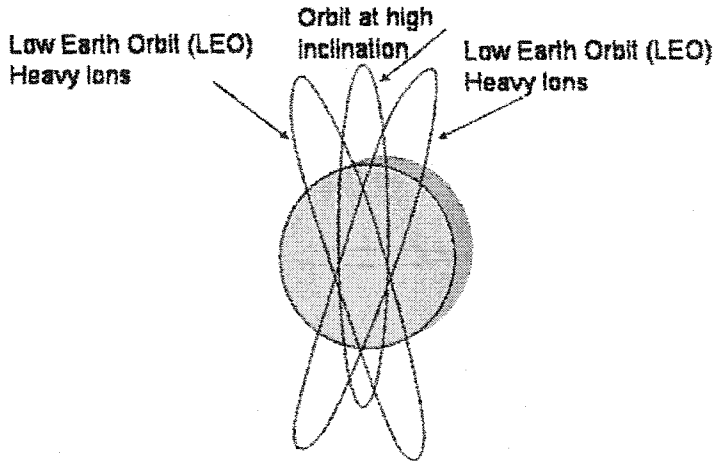

Figure 1b: Heavy ions from galactic cosmic rays come in along the polar magnetic field lines. They are a particular problem for low earth, high declination orbiting spacecraft.

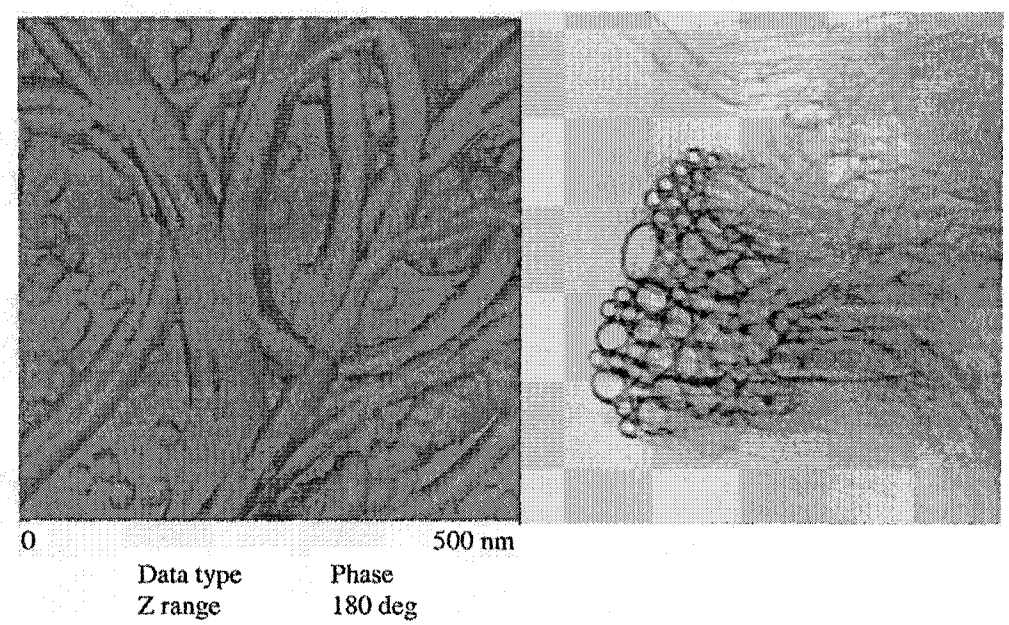

(a) (b)

Figure 2: Examples of ropes of single-wall carbon nanotubes (a) Tapping Mode AFM image of ropes dispersed on a gold substrate. Each "strand" is actually 15-20 close-packed single-wall carbon nanotubes. (b) Cross sectional HRTEM from the Smalley group photo gallery showing how the individual tubes are arranged within a typical rope (http://smalley.rice.edu/index.php?topgroupid=1&groupid=10).

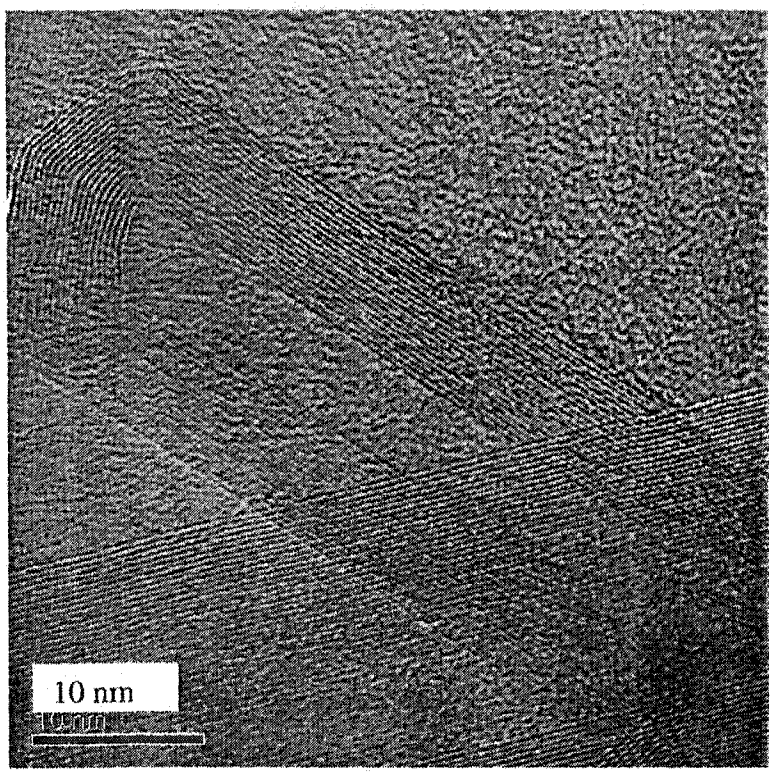

Figure 3: HR TEM Image of a typical Multi-wall CNT showing individual layers

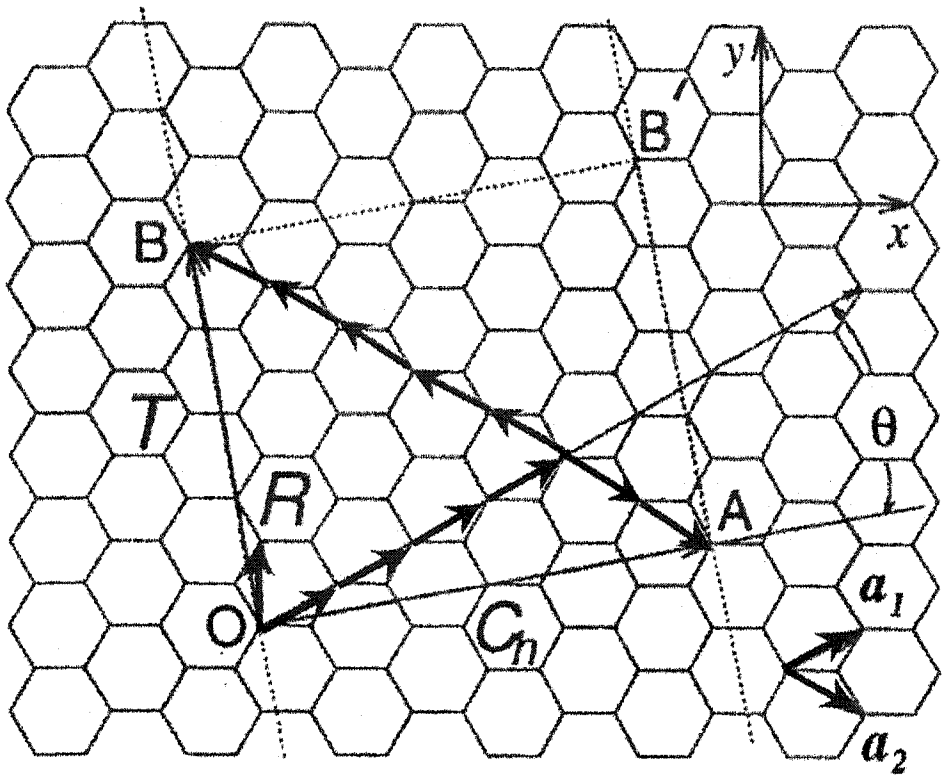

Figure 4: Definition of the Chiral (C_h), Translational (T) and Symmetry (R) Vectors

Vectors OA and OB define the chiral vector (C_h) and the translational vector (T), respectively. R is the symmetry vector. The Figure corresponds to C_h=(4,2), T=(4,-5) and R=(1, -1). The rectangle OABB' defines the unit cell of the nanotube. (Taken from R. Saito, G. Dresselhaus and M.S. Dresselhaus, "Physical Properties of CNTs", Imperial College Press, 1998)

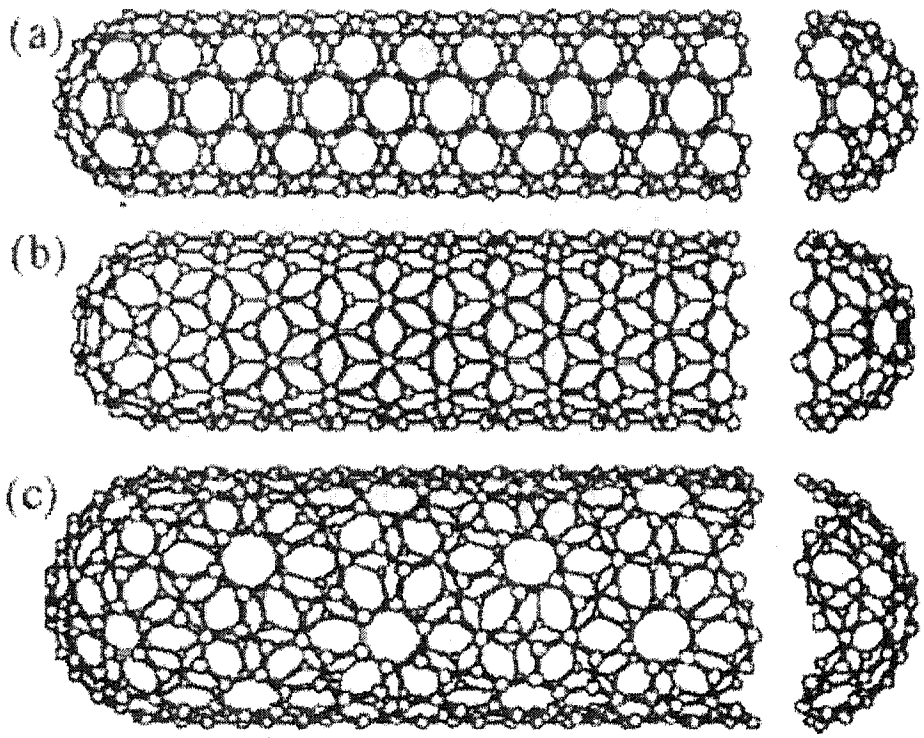

Figure 5: The Different Types of Chiral Structures of Carbon Nanotubes

(a) Armchair nanotube (carbon atoms are perpendicular to the nanotube axis) (b) Zigzag nanotube (c) chiral nanotube (Taken from R. Saito, G. Dresselhaus and M.S. Dresselhaus, "Physical Properties of Carbon Nanotubes", Imperial College Press, 1998)

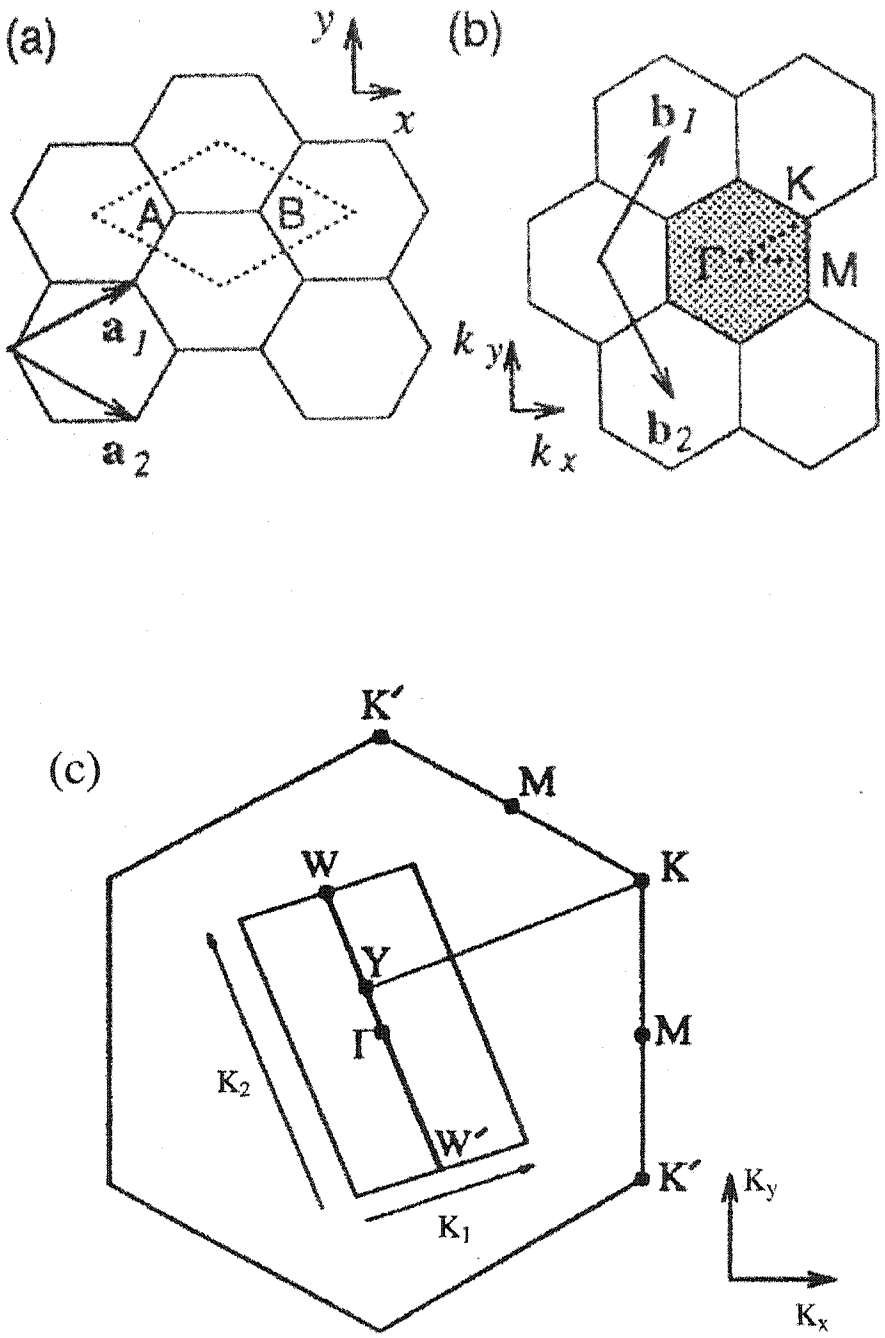

Figure 6: Relationship between Wave Vectors in a Carbon Nanotube. (Taken from R. Saito, G. Dresselhaus and M.S. Dresselhaus, "Physical Properties of Carbon Nanotubes", Imperial College Press, 1998)

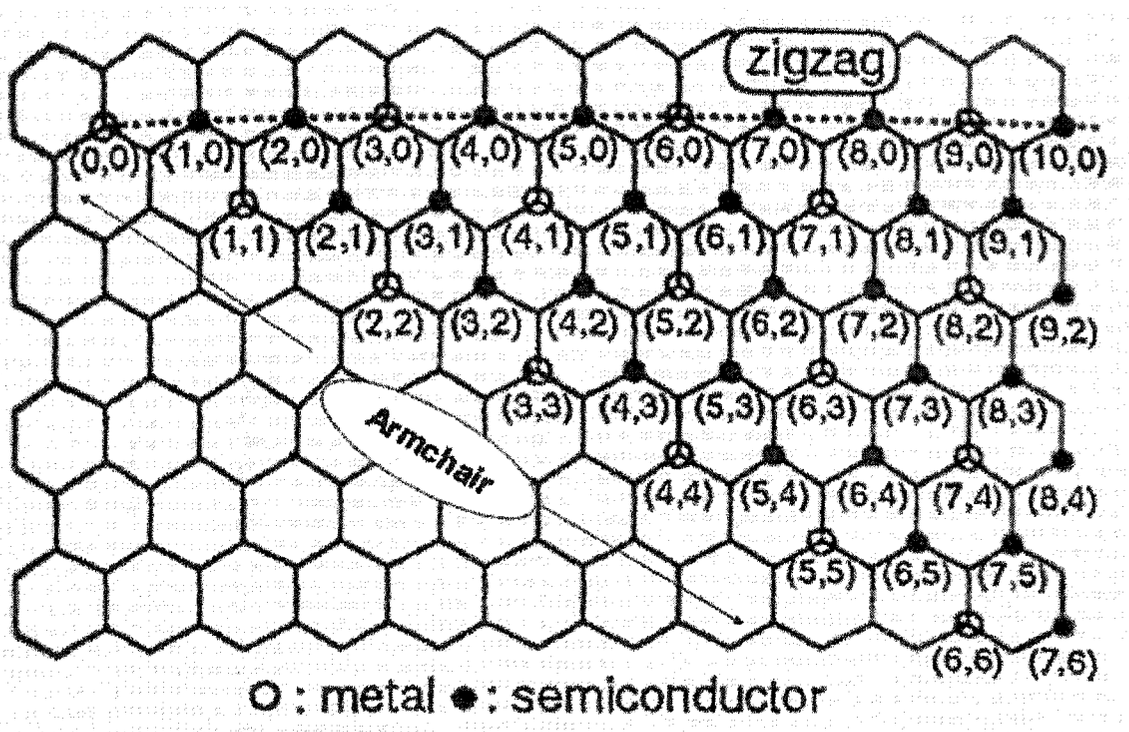

Figure 7: Indices vs. Conductivity for Carbon Nanotubes.
(Taken from R. Saito, G. Dresselhaus and M.S. Dresselhaus, "Physical Properties of Carbon Nanotubes", Imperial College Press, 1998)

Mechanical Properties of CNTs

The Young's modulus of a material defines the stiffness or strength of a material. The Young's modulus of single-wall CNTs was reported to be as high as a few TPa using innovative in-situ methods in TEM. Multi-wall CNTs have a high young's modulus, or elastic modulus, which is the ratio of stress over strain, of several Gigapascals (GPa) in the direction of the tube axis. The TEM method [15] of measuring Young's modulus of CNTs utilizes thermal energy to cause the nanotubes to vibrate. More specifically, the amplitude of the thermal oscillations is measured using TEM by utilizing several images taken using a CCD camera. Then, treating the nanotube as a cylindrical cantilever, the vibration energy W, is related to the effective spring constant k by $W = \frac{1}{2}ku_n^2$. Then since the effective spring constant is a function of the Young's modulus, one can simply solve for the Young's modulus. The Young's modulus is a function of a CNT's diameter and helicity.

Another measure of strength of a material is the bending modulus. The bending modulus is a measure of how much a material can be bent before it breaks. In another set of experiments in the TEM, by using a frequency variable oscillating voltage supply, the resonant frequency was determined. This is because resonance is selective based on the nanotube's dimensions. Then the resonant frequency, f_i, of the CNT was used to determine the bending modulus because it is dependent on the Bending modulus, E_β, and is given by:

$$f_i = \frac{\beta_i^2}{8\pi}\frac{1}{L^2}\sqrt{\frac{(D^2 + D_1^2)E_\beta}{\rho}} \qquad (7)$$

where D is the outer tube diameter, D_1 is the inner diameter and L is the length of the nanotube. These parameters can be determined from a TEM image. The other parameters are constants. The density of carbon is given by ρ, β_1=1.875 and β_2=4.694, for the first and second harmonics.

After a bit of rearranging, one finds that the Bending modulus, E_β, as a function of the resonant frequency and other parameters is given by the following equation:

$$E_\beta = \frac{f_i^2 64\pi^2 L^4 \rho}{\beta_i^4 (D^2 + D_1^2)} \tag{8}$$

Hence, the once the resonant frequency, f_i, of the CNT is found, one can determine the bending modulus.

A third measure of strength is the strain energy. The strain energy, E_σ of the single-wall CNT, when considered as a graphene sheet, is given by:

$$E_\sigma = \frac{\pi E T d_f^3}{6 d_t} \tag{9}$$

d_t is the diameter of the nanotube, T is the length of the CNT per 1D unit cell in the direction of the nanotube axis and E_σ is the Young's or Elastic modulus of the sheet. Carbon is very unique in that it allows for hybridization of its σ and π orbitals. The great strength of CNTs in the direction of the nanotube axis comes from first, the strength of the double bond between the carbon atoms due to the σ bonding, π bonding and lastly,

weak interlayer interactions. The strain energy experienced by a CNT increases with decreasing diameter of the CNT. CNTs are very flexible in the direction perpendicular to their axis.

CNTs also have the ability to store elastic energy, which is the potential energy stored when a material is deformed. The first contribution to elastic energy in CNTs is due to the σ electrons. The second contribution comes from π electrons.

CNTs, in comparison with trans-polyacetylene, experience only a limited Peierl's distortion. Peierl's distortion refers to the tendency of a double-single-bond combination to freeze into a series of quantum wells and barriers rather than hybridize into a delocalized electronic state, as shown in Figure 7. Peierl's distortion causes a metal-insulator transition, which combines a mechanical effect with an electronic outcome. Peierl's distortion has been a serious limitation in attempts to manufacture carbon-based molecular electronics, such as polyacetylene-based molecular wires. However, it does not look to be a serious issue in CNTs. In CNTs, the Peierl's distortion is applicable only to metals and hence to only one third of the CNTs, which are metallic in nature. Energy analyses indicate that, though the metallic energy bands are unstable under the Peierl's distortion, the induced energy gap is very small, $< 10^{-3}$ eV [13]. A distortion of 10^{-3} eV would not be significant in a 0.5-1 eV bandgap measurement, and even if observed could be due to other causes. No serious Peierl's distortion problems have been reported in the literature to date.

Thus, CNTs have many exciting potential applications due to their excellent mechanical properties, namely high Young's modulus, high aspect ratio, and considerable strength and flexibility. Multi-wall CNTs are already being used as Scanning Probe Microscopy tips [16] and could possibly be used as linear bearings [17], and coaxial conducting wires or capacitors. The formation of CNTs into space elevators [18] has also been theorized.

These excellent electronic and mechanical properties of CNTs have spurred research into other potential applications such as a battery [19-20], a flow sensor and a beam source for TEM [21-23]. Additionally, their high aspect ratio inspired research into their potential use as field-emission displays, resulting recently in a highly compact CNT-based x-ray device for portable medical applications [24].

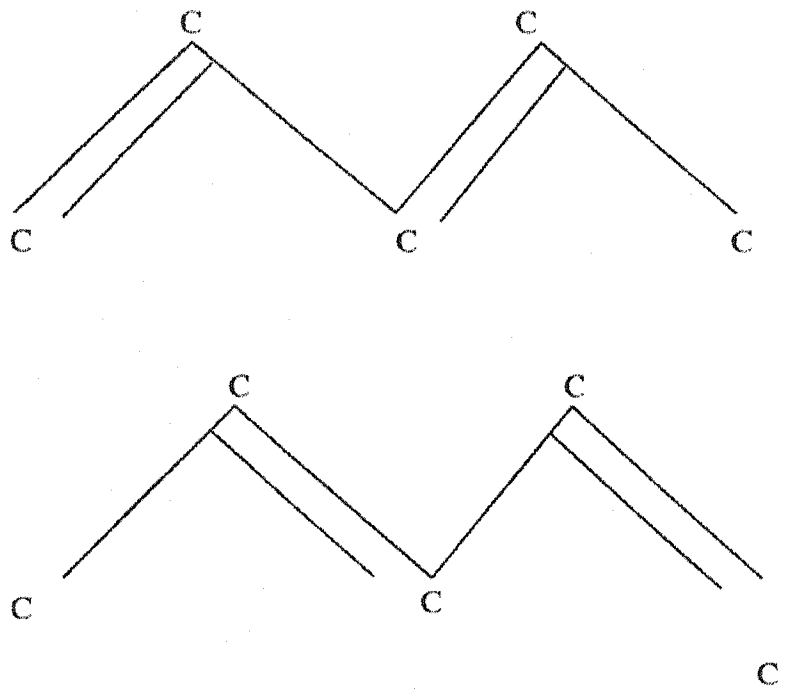

(a)

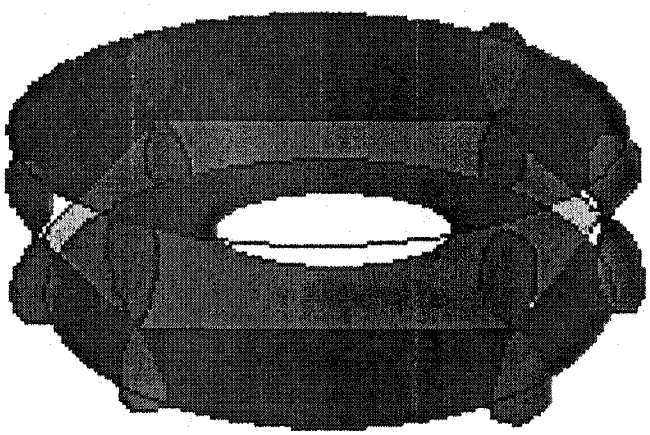

(b)

Figure 8: PEIRELS DISTORTION (a) TRANS-POLYACETYLENE experiences a large Peierl's distortion while (b) Benzene is almost completely delocalized. CNTs exhibit only a small Peierl's distortion.

Theoretical Growth Mechanism of CNTs

The axial growth mechanism (length-addition) of CNTs had been under debate for many years. The two most widely debated growth models for the growth of CNTs were the closed-growth and the open growth model. The closed growth model assumes low growth temperature (~1100°C) and that the nanotube is always capped. According to this model, growth occurs through the absorption of a C_2 dimer near a pentagon in the cap of the nanotube. In the open growth model, a high temperature is assumed, and growth is also achieved by the addition of a C_2 dimer. Capping to an open end occurs eventually due to the formation of a heptagon-pentagon defect pair, as illustrated in Figure 8. These heptagon-pentagon pair defects are also known as Stone-Wales defects.

Some support for the open growth method comes from the direct observation of open-end CNTs [25]. Another piece of evidence which supports this model is the observation of CNTs inside larger diameter nanotubes. CNT encapsulated C_{60} fullerenes ("bucky balls") have also been produced by pulsed laser vaporization, the majority of which involve 1.4 nm diameter CNTs, possibly due to the favorable van der Waals separation of 0.3 nm [26]. There has been no experimental validation of the closed growth model. For both of these carbon addition mechanisms, a metallic catalyst need not be present. A catalyst was not used for the multi-wall CNTs from the NASA Goddard Space Flight Center.

Other proposed growth models included the polyyne ring nucleus model [27] and the Liquid-Metal-Solid (LMS) model [28]. To date, these methods rely on the presence of a

metallic catalyst. In the polyyne ring nucleus model, growth occurs when small monocyclic rings (C10-C60) join to form polycyclic rings and convert to either fullerenes or back to monocyclic rings in the presence of cobalt (Co) in combination with one of three other catalysts: sulfur (S), bismuth (Bi) or lead (Pb). In the presence of cobalt, the other catalysts sulfur, bismuth or lead tend to increase the yield of single-wall CNTs and modify the diameter distribution [29]

The LMS model has been verified but only applies to the specific case where a catalyst was deposited on a substrate and growth was conducted using plasma. In the LMS model, essentially the carbon is absorbed into the catalyst and then upon saturation the carbon is extruded in the form of a nanofiber or nanotube. We have evidence that suggests that the carbon components of the CNT-Si nanowire heterostructures produced by the experiments conducted at the University of Michigan were grown according to an LMS model.

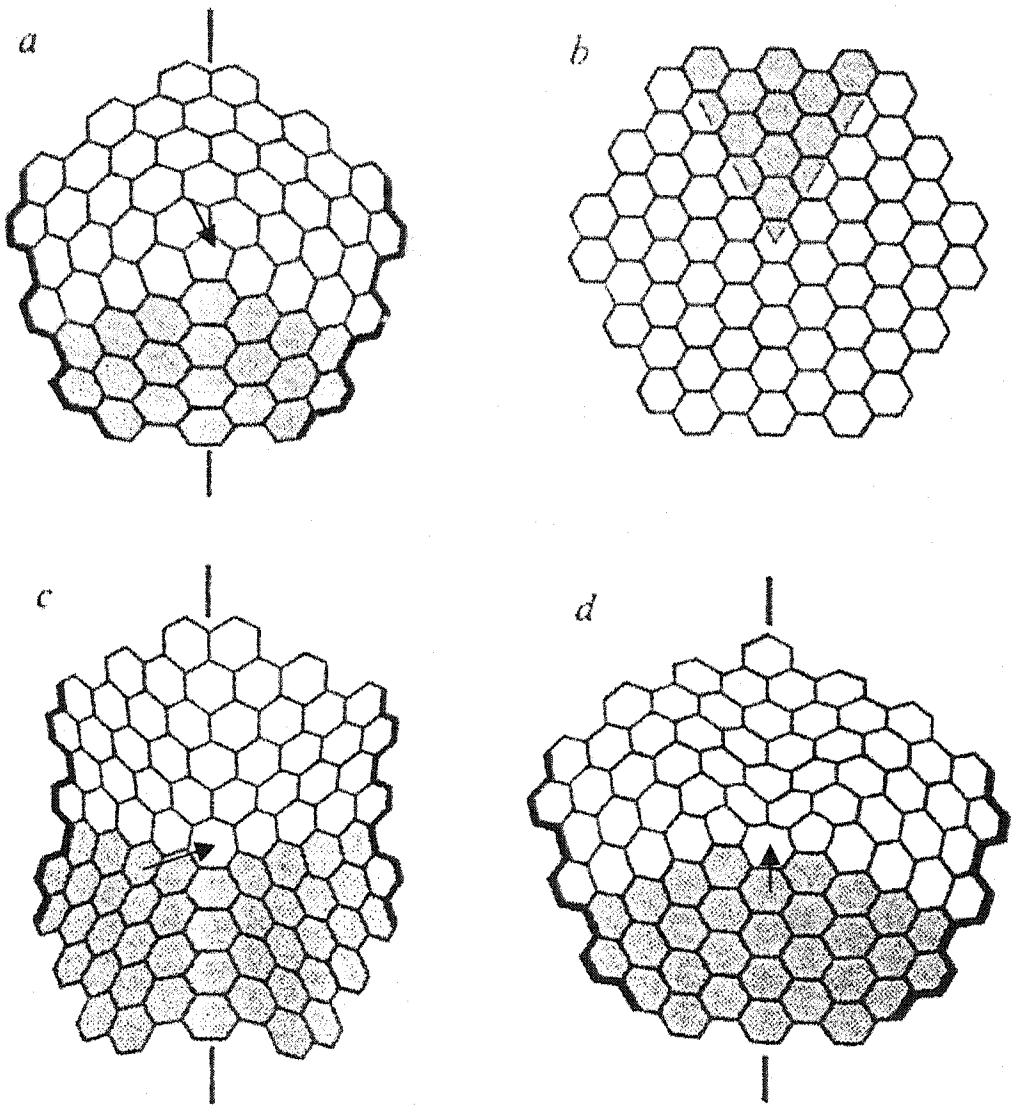

Figure 9: Formation Mechanism of End Caps in Carbon Nanotubes

Show are the formation of a disclination in carbon nanotubes via the a) addition of a pentagon, b) removal of shaded hexagons, c) addition of a heptagon, highlighted in red and d) addition of two pentagons and a heptagon. Arrows are drawn to allow for easier identification (Taken from M.S. Dresselhaus, G. Dresselhaus, A. Jorio et al, "Raman spectroscopy on isolated single wall carbon nanotube", Carbon Vol. 40, pp. 2043-2061 (2002)

CHAPTER 2

ANALYSIS METHODS

The CNT-silicon nanowire heterojunctions and the CNTs pre- and post-irradiation were investigated using four methods: (1) Micro-Raman spectroscopy and Surface-Enhanced Raman spectroscopy, (2) scanning electron microscopy (SEM), (3) transmission electron microscopy (TEM) and high-resolution transmission electron microscopy, both with selected area diffraction, and (4) atomic force microscopy (AFM). These four methods will now be discussed in further detail.

Raman Spectroscopy/Surface Enhanced Raman Spectroscopy

Raman spectroscopy reveals the bonding structure and the degree of purity of a volume of a material equal to the spot size times the penetration depth of the laser beam. There are two methods used in Raman spectroscopy: Anti-Stokes and Stokes. For this project, the Stoke's method was used, i.e., a laser beam is incident on a material, induces lattice vibrations, or phonons, at certain frequencies, and causes the photon from the laser beam to lose energy. This loss of energy to the sample causes a shift in the wavelength of the photon. This shift is then detected by the monochromator. This results in peaks at characteristic shifts away from the original wavelength of the beam. Sharp peaks indicate a highly ordered material, whereas broad peaks are due to amorphous material. This allows us to differentiate between different morphologies of carbon, such as SWCNTs and MWCNTs.

The Micro-Raman system used for this project is shown in Figure 10. It consists of an Argon-ion laser from Coherent, an optical microscope, an Electron Tubes 9124B photo-multiplier tube and a Jarrell-Ash 25-100 series double Czerny-Turner monochromator set up in back-scattering configuration. The Raman system and the software for controlling the Raman system were designed and built by Joerg Mossbrucker for his Master's thesis project [30]. The wavelength at which the CNTs were examined was 514.5 nm. The Raman spectra were deconvolved with Lorentzian peak amplitudes using PeakFit® software. For the Raman investigations the photomultiplier tube was air-cooled, and the room lights were turned off, to reduce noise. The samples were placed on the microscope stage and the laser beam was focused to a spot size of approximately 30 microns using the 60x objective.

For the Tubes@Rice single-wall nanotubes, at the 514.5 nm wavelength the two strongest tangential modes occur at the Raman shifts of 1567 cm^{-1} and 1591 cm^{-1}. The peaks occur at the same Raman shifts at the 488 nm wavelength. However, the peaks have a smaller full width at half maximum (FWHM) and are sharper. The D-band or "disorder peak" for CNTs and planar graphite occurs at 1350 cm^{-1} and is a broad peak. For silicon, at the Raman peak occurs at 523.286 cm^{-1} and does not overlap with the carbon peaks in any experiments where both might be present. Multi-wall peaks have a Raman shift at about 1580 cm^{-1}.

The radial breathing modes of CNTs occur at $248/d_t$ cm^{-1}, where d_t is the diameter of the nanotube [13]. This spectral information was unfortunately available to us due to the

overlap of the high brightness laser line for the 514.5 and 488 nm wavelengths. An attempt to analyze the breathing modes using the HeNe laser was also unsuccessful. 633 nm (red light) has a stronger coupling to carbon sp2 bonds than either 514.5 nm or 488 nm wavelengths. However we found that our PMT lacked the requisite sensitivity in the red range.

Surface-Enhanced Raman Spectroscopy employs the use of metallic nano-particles (colloidal silver or gold) to enhance the response of the sample to the laser excitation. The enhancement is primarily due to large local electromagnetic fields which come from resonant optical excitation of surface plasmons (packets of electrons) [31] That is, energy transfer between photons and the photons which occurs only when the wavelength where the quantum energy carried by the photons exactly equals the quantum energy level of the plasmons.

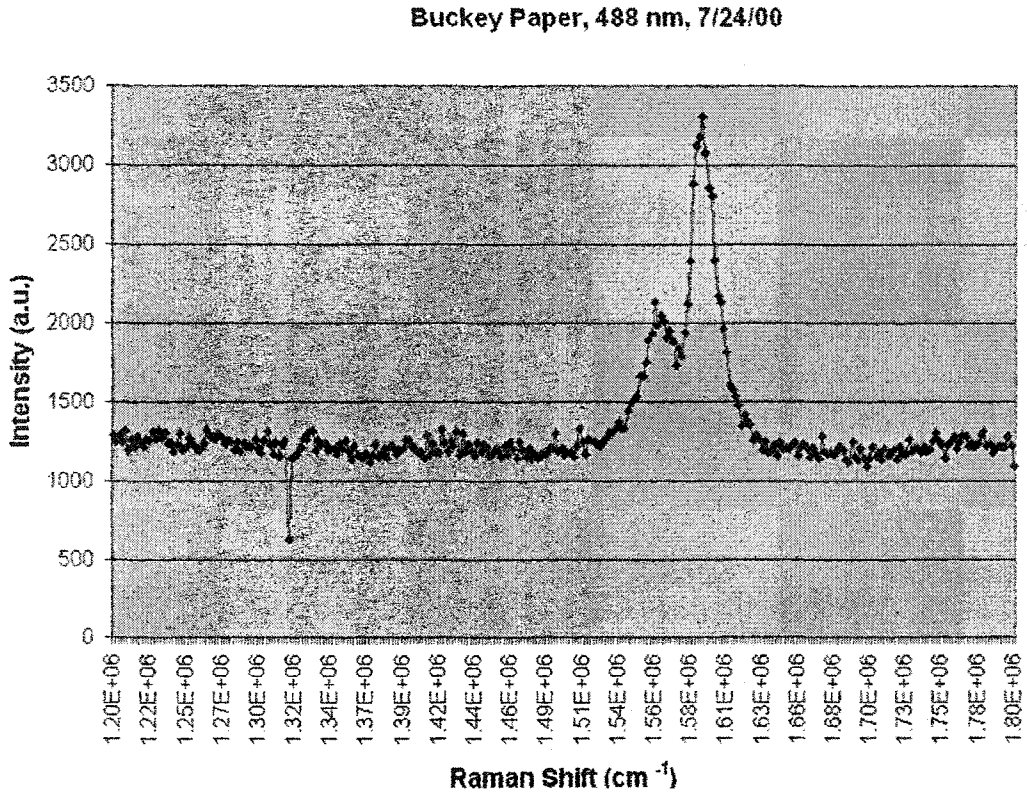

Figure 10: Raw Raman Spectra Taken at 488 nm Showing Tangential Modes for Tubes@Rice

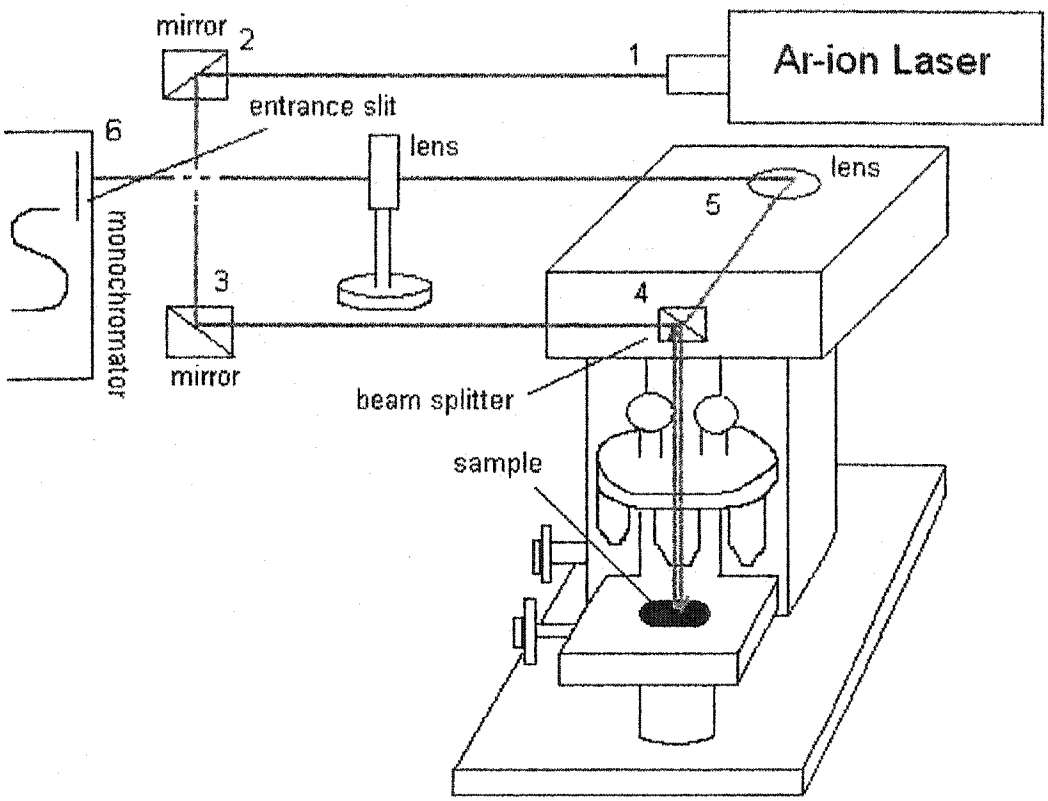

Figure 11: Schematic of Raman System in Backscattering Configuration: Numbers 1-6 represent the order in which the light traverses the beam path

Scanning Electron Microscopy

Scanning electron microscopy (SEM) allows surface analysis of materials at the micron to nanometer scale. For the scanning electron microscope used in this project, the electron beam is generated by an electron gun, guided in a raster pattern down the column by two scanning coils in the objective lens and the electrons hit the atoms in the sample, resulting in various types of scattered electrons. They are secondary, back-scattered, and Auger electrons. Secondary electrons are low energy electrons excited from 100 nanometers or less within the sample, back-scattered electrons are high-energy electrons which are reflected by an angle greater the 90°. These scattered electrons are then detected by an Everhart-Thornley detector. The front of the detector is a Faraday cage. Secondary electrons, once inside the Faraday cage, are then attracted to the scintillator which is the second component of the detector, across which a 12 kV voltage is applied. The Scanning Electron Microscope was useful for determining the distribution of the CNTs in the Si-CNT heterostructure sample.

The Scanning Electron Microscopes used for this project were the CamScan 44FE Field Emission Scanning Electron Microscope and the Hitachi S-4700II Field Emission Scanning Electron Microscope. A field-emission scanning electron microscope differs from a regular scanning electron microscope in that emission from a sharp-pointed emitter occurs through application of a high electric field. Generally field-emission scanning electron microscopes allow for higher resolution and induce less damage to a sample.

High-Resolution Transmission Electron Microscopy/Transmission Electron Microscopy

In TEM, an electron beam is generated by an electron gun. For the Hitachi H-800 (E=200 KeV, λ=.00251 nm), the electron gun is thermionic, *i.e.*, the electron beam is produced by the resistive (thermionic) heating of a tungsten filament. The electrons are sent down a column, hit atoms in the sample, whereby the electrons are scattered in a variety of ways (diffraction, reflection, and backscattering). Forward scattered electrons are the primary source of signals used in the TEM. High-Resolution transmission electron microscopy (HR-TEM) is used to analyze the atomic layer structure of nanoscale materials. HR-TEM is therefore valuable in the study of CNTs because it reveals their structure in atomic scale, their crystallinity and various mechanical properties. Transmission electron microscopy (TEM) provides structural information with resolution equal to that of Atomic force microscopy (AFM). HR-TEM has higher resolution than either AFM or TEM to atomic plane spacings.

Contrast in a TEM/HR-TEM is in three forms: amplitude, diffraction and phase contrast. Amplitude contrast occurs when using a small objective aperture, excluding all electrons except those of either the transmitted electron beam or the diffracted beam. Diffraction contrast occurs when you have a two beam condition, so that you have only the main beam and one strongly diffracted beam. Phase contrast occurs due to differences in the phases of the electron waves scattered from a sample. A phase contrast image is taken with a large objective aperture. Regions of the sample with higher mass density or which are strongly biased will scatter more electrons, and therefore appear dark in the image

[32]. How much information in reciprocal space is transferred to the image is dependent on H(u), the contrast transfer function. H(u) then is the product of the aperture function, envelope function and the aberration function. The phase distortion function is $\chi(u)$.

$\chi(u)=\frac{\pi}{2}C_s\lambda^3u^4+\pi\lambda\Delta fu^2$, where C_s is the spherical aberration coefficient, λ is the wavelength of the electron, Δf is the defocus value, and u is the magnitude of the unit vectors in reciprocal space. $\chi(u)$ is valuable because it allows one to determine the effect of spherical aberration, acceleration voltage and defocus value on the resolution.

In the case of the CNT-Si nanowire heterostructures, the amplitude contrast allowed ready differentiation between the silicon, iron and carbon components. The accuracy of the measurement of CNTs using TEM varies with the diameter of the tube. It has been reported that in general, based on simulations of TEM images, for CNTs with diameter larger than 1.0 nm in diameter, the estimate of the tube diameter agrees to within 10% of the value, whereas for those sub nanometer in diameter, the difference could be as large as 30% [32].

The CNTs were prepared for TEM and HR-TEM by ultrasonicating in ethanol, and then pipetting onto 3 mm diameter mesh copper grids covered with holey carbon film. The holey carbon film was prepared according to the procedure outlined in Appendix A. The primary benefits of holey carbon film are that it is stable under the electron beam, prevents charging of the material being investigated and supports more material than the copper grid alone.

Calculation of diffraction patterns for CNTs

Selected area diffraction was an important tool for our analyses. The diffraction pattern in general reveals the crystallinity and the identity of a material because the diffraction patterns for materials differ significantly for amorphous, polycrystalline and crystalline materials. Amorphous materials produce rings for the diffraction pattern, due to the random orientation of the atoms, polycrystalline materials produce speckled rings, and crystalline materials produce spots. If the crystal does contain defects, then streaks are produced. One can calculate the relevant parameters of interest, such as the lattice parameter and symmetry of a crystalline material using the diffraction pattern.

As previously mentioned, the brillouin zone of the CNT is comprised of rectilinear segments inside the hexagon of carbon atoms. The reciprocal lattice vectors, b_1 and b_2 for the CNT, are

$$b_1 = \left(\frac{1}{\sqrt{3}},1\right)\frac{2\pi}{a}, b_2 = \left(\frac{1}{\sqrt{3}},-1\right)\frac{2\pi}{a}$$

The various lattice spacings, d, for different orientations of a CNT or any crystal, can be found via the simple equation $Rd=\lambda L$, where R is the distance between diffraction spots or rings on a TEM diffraction pattern, L is the camera length, and λ is the wavelength of the electron. For CNTs, HR-TEM reveals whether they are multi-wall or single-wall.

The expected diffraction pattern for CNTs of different indices can be calculated by using the following equation given in a previous report [33]:

$$A(k) = f(k)\sum_{j}\exp\left[ik \cdot R_j\right] \equiv \sum_{n,m} A_{n,m}(k)$$

$$A(k) = f(k)\sum_{n,m}\delta\left[k_z - 2\pi\left(\frac{n}{P} + \frac{m}{p}\right)\right]J_n(k_\perp r)\exp\left[i\left[n\left(\psi_k - \varphi + \frac{\pi}{2}\right) + k_z z\right]\right] \quad (11)$$

where $f(k)$ is the carbon structure factor of the electron or X-ray, R_j are the atomic positions along the helix, (n,m) are two integers representing the indices of the CNT, $\bar{k} = (k_x, k_y, k_z)$ is the wave vector transfer, $k_\perp = \sqrt{k_x^2 + k_y^2}$, $\psi_k = \tan^{-1}\left(\frac{k_y}{k_z}\right)$, J_n is the nth order cylindrical Bessel function (r,φ, z) are cylindrical coordinates of the "initial" atom of the helix of radius r, pitch P and atomic repeat distance p in the z-direction.

The one disadvantage posed in using TEM and HR-TEM is that although they allow for highly detailed investigation of the structure of a material, due to the minute amount of the sample examined, it does not allow one to determine the uniformity of properties of the majority of a material.

Atomic Force Microscopy

Atomic force microscopy (AFM) is a form of scanning probe microscopy (SPM), which provides structural information with tens of nanometers scale resolution. In AFM, a sharp tip made of SiN or silicon, which is attached to a cantilever, is brought close enough to the sample so that the atomic orbitals of the tip interact with those of the sample. The tip is raster scanned across the sample by a piezoelectric scanner. A laser

beam is reflected off the back of the cantilever which holds the tip and detected by a four-cell photodiode. Therefore, when there is a change in the position of the tip, there is a change in the strength of the signal being detected by the photodiode quadrants. The topographical image is formed via the stored vertical position of the piezoelectric scanner at each (x,y) point which was required to maintain either a constant height or a constant deflection or a constant oscillation amplitude near the cantilever resonant frequency (Tapping Mode, discussed below). Constant values are maintained through the use of a feedback loop.

There are two modes of AFM: Tapping Mode™ and contact mode. In Tapping Mode™, a micro machined silicon tip at the end of a silicon "diving board" cantilever is used. The diving board is oscillated near its natural resonant frequency by means of a small external signal. When the tip nears the sample surface, interactions with the sample induce small changes in the oscillation frequency, the rms amplitude of which is detected by the photodetector, and plotted as (z: x,y). The phase difference between the natural resonant and interaction frequencies can also be plotted ($\Delta\phi$: x,y) and this information is particularly sensitive to material composition differences, and also to edges. This work was performed in Tapping Mode most of the time. In contact mode, a micro-machined SiN tip on the back of a triangular non-oscillating cantilever is used. Variations in the choice of the spring constant k of the cantilever allow flexibility in examining different surfaces, where k is the same as that in Hooke's law, $F=kx$. The height, or the deflection, of the tip with respect to the sample surface is kept constant.

AFM, because of its high-resolution capability, provides detailed information as to the surface structure of individual nanotubes as well as the presence of defects which go through to the surface. The phase image reveals differences in the composition of a sample. Atomic Force microscopy is useful for structural and compositional analysis of the CNT and carbon nanofiber surfaces.

Scanning probe microscopy was conducted using the Nanoscope IIIa Multimode SPM System from Veeco Metrology Group/Digital Instruments, operated in ambient air.

CHAPTER 3

SYNTHESIS AND SAMPLE PREPARATION METHODS

The CNTs examined for this project were synthesized by three different methods. One set of CNTs were commercially produced by Tubes@Rice and Carbon Nanotechnologies via the HiPco method (high pressure carbon monoxide (CO) decomposition) and produced exclusively single-wall CNTs. Another set of CNTs was produced at the NASA Goddard Space Flight Center using the carbon arc method in a helium atmosphere without a catalyst. This method produced exclusively multi-wall CNTS with well-defined walls composed of single graphene layers. The third method involved growth of MWCNTs as part of a MWCNT-Silicon nanowire heterostructure using plasma deposition in an inductively coupled plasma (ICP) Reactor. Two other hollow core carbon fibers with well-defined wall structures were also investigated for comparison with the CNTs. These were: Electrospun carbon nanofibers and vapor grown carbon fibers. All synthesis conditions will now be briefly described.

Production of Single-Wall Nanotubes

Single-wall CNTs, from the Rice University spin-off companies Tube@Rice, now called Carbon Nanotechnologies [http:// cnanotech.com/pages/about/4-1_background.html], were produced via the HiPco process and suspended in toluene. In the HiPco process, flowing CO is mixed with $Fe(CO)_5$ through a heated reactor. The reaction produces iron clusters, which then serve as catalyst particles for CNT growth. More specifically the solid carbon is produced via the following reaction:

$$CO + CO \xrightarrow{Fe} C(s) + CO_2 \qquad (10)$$

The CNTs are then suspended in a toluene solution. Before analysis by our group they were purified and formed into "Bucky Paper" according to the procedure reported by Rinzler et al [34]. In this process the Tubes@Rice suspended in toluene were first refluxed in 2-3 M nitric acid for 45 hours. After the reflux, the CNTs were placed in a container and allowed to settle and the brownish-yellowish supernatant liquid on the top of the container was decanted. This was then followed by suspending the CNTs in deionized water via ultrasonication, allowing the CNTs to settle and then decanting the supernatant liquid and repeating the previous steps two or three times until the liquid is dark throughout. Finally, the solution was dispersed in NaOH via ultrasonication and then vacuum filtered through a membrane and allowed to dry, forming the "bucky paper"

Production of Multi-wall Carbon Nanotubes at the NASA Goddard Space Flight Center

To produce the multi-wall CNTs at the NASA Goddard Space Flight Center, a graphite rod was welded at a steady rate with a Helium pressure of 50 psi and a current of 19 Amps. The catalyst requirement was relaxed. The relationship between amount and quality of growth and experimental parameters including pulse width, current amplitude and helium pressure, has been under development. The specimens utilized in the radiation experiments were also subjected to a unique (patent pending) filtering process, which resulted in high MWCNT yields. Figure 32 shows examples of NASA GSFC MWCNTs, indicating good defect free walls between 5-20 layers in thickness.

Production of Multi-wall Carbon Nanotube-Si Nanowire Heterostructures (Collaborative Effort, University of Michigan and Michigan State University)

Carbon nanostructures of approximately micron-scale lengths were grown in an inductively coupled plasma system, using a 20-nanometer layer of iron catalyst on a p-type (100) silicon wafer in methane-hydrogen-argon plasma. The carbon nanostructures were shown to be multi-wall CNTs and hollow core vapor grown carbon nanofibers. Simultaneously, tapered silicon nanowires were etched that retained the (100) orientation and crystallinity of the original silicon substrate. Increasing reactor times resulted in a progressive etch of the silicon nanowires, but no change in the approximately micron-scale lengths of the CNTs and nanofibers. Junctions were observed between the silicon and carbon nanostructures.

The simultaneous growth/etching was achieved in an inductively coupled plasma system. Inductively coupled plasmas (ICP) have high radial uniformity and low pressure/low temperature operating characteristics [42] which make them attractive for large-scale applications. The inductively coupled plasma system was based on a modified Gaseous Electronics Conference (GEC) Reference cell [43]. The original GEC reactor had two parallel electrodes, 2.54 cm apart. The bottom electrode was biased with a 13.56 MHz radio frequency (RF) power supply at 50 Watts. In the modified cell, the top electrode was replaced by a 5-turn coil that was also powered by a 13.56 MHz RF power supply at 475 Watts. The pressure of the gas mixture was 100 mTorr with 87% Argon, and 6.5% methane and 6.5% hydrogen. Argon was used to sustain the plasma in the inductively coupled mode. Further details are reported in reference [44].

Samples were prepared by forming a 10-20 nm thick Fe layer on a p-type (100) silicon substrate, using laser ablation [45-46]. Individual depositions were carried out over time periods of 1 hour 0 minutes, 3 hours 10 minutes, and 5 hours 23 minutes.

This work was performed as part of a collaborative effort with the University of Michigan using the University of Michigan Gaseous Electronic conference (GEC) Reference Cell, with its unique Spatially Resolved Optical Emission Spectrometer (SROES). Nanoscale heterojunctions between silicon and other nanotube/nanowire materials may have important applications in nanoscale electronic devices, and as interfaces between new nano-materials and conventional silicon electronics. Formation of such nano-heterostructures by means of a common catalyst and a Liquid-Metal-Solid (LMS) growth mechanism for both parts of the heterostructure have been recently reported [35-41].

Production of Electrospun Carbon Nanofibers

The pre-irradiation carbon nanofibers were electrospun from polymer monomers. The basic components of a typical electrospinning set-up are shown in Figure 33. The ES-CNF's in the present experiment were about 200 nm in diameter, but our collaborative group [60] has also spun fibers down to about 25 nm in diameter.

Electrospinning involves the application of electrostatic force between polymer monomers in solution kept in a narrow bore pipette or a syringe (capillary), and a metal electrode kept at a suitable distance [47]. A charged drop of monomer + solution is

formed at the tip of the capillary, sometimes by tilting the syringe. With an increase in electric potential, the charged drop of polymer solution formed at the tip of the capillary is deformed into a cone, know as "Taylor's cone". At a critical field, the force due to the electric field overcomes the surface tension forces holding the droplet, and the solution starts flowing towards the collecting electrode in the form of a charged jet. While in transit, most of the solvent molecules evaporate away and the different polymer strands in the jet separate out due to mutual repulsion ("splaying"). When these reach the collecting electrode the diameters of the self-assembled fibers are in the range of a few micrometers to nanometers. A basic electrospinning set-up and examples of electrospun carbon nanofibers are shown in Figure 33. The electrospun carbon nanofiber samples from MSU were provided by Professor Melvin S. Schindler, Department of Biochemistry and Molecular Biology, Michigan State University.

Production of Vapor Grown Carbon Fibers

Well-graphitized vapor grown carbon fibers were obtained from G. Tibbett's research group at General Motors Research and Development Center in Warren Michigan. These were produced by carbon vapor feedstock thermal decomposition, flowed over a metallic catalyst bed, as described in Reference [48]

CHAPTER 4

NEW HETEROSTRUCTURE FORMATION MECHANISM

The formation of silicon and carbon hetero-nanostructures in an inductively coupled plasma system by a simultaneous growth/etching mechanism was reported by our group in Reference [42]. Multi-wall CNTs were grown during one, three and five hour depositions while tapered silicon nanowires were progressively etched. The carbon and silicon nanostructures and the interfaces between them were studied by electron microscopies and micro Raman spectroscopies. This method has potential for large-scale controlled production of nano heterostructures without the requirement of a common catalyst.

Scanning electron microscopy (SEM), transmission electron microscopy (TEM) with selected area diffraction (SAD), high-resolution transmission electron microscopy (HR-TEM) with Energy Dispersive x-ray Spectroscopy (EDS), and micro-Raman Spectroscopy and Surface Enhanced micro Raman Spectroscopy (SERS) were used to characterize the resulting carbon and silicon nanostructures. The SEM was performed using a Cam Scan 44FE. The TEM was performed using a Hitachi H-800 Transmission Electron Microscope operated at 200 kV and the HR-TEM was performed using a JEOL JEM 2010F operated at 200 kV, at Michigan State University. A JEOL 4000 EX operated at 400 kV at the University of Michigan was also used for some of the HR-TEM analysis. Samples were prepared for TEM/HR-TEM by wetting the surface of the sample with ethanol and gently scraping, followed by dispersing the ethanol and sample via a pipette onto holey carbon film TEM grids.

The micro Raman spectroscope consisted of a 0.75 m double monochrometer coupled with an optical microscope, operated in backscattering configuration, with an argon ion laser as the excitation source. 514.5 nm and 488 nm excitation wavelengths were both used in these investigations. SERS spectroscopy was performed as described in Ref. [48], using 20 nm of sputtered gold on a glass substrate.

Scanning Electron Microscopy Results

For the three deposition time periods, SEM images taken at 0° tilt showed a uniform sparse coverage of fibrous nanostructures on a dotted background. A typical example from the five-hour sample is shown in Figure 12. The coverage appeared to be uniform over roughly 4 cm^2 sample areas. Upon tilting to 40°, it became apparent that the dotted backgrounds were tips of tapered nanostructures perpendicular to the surface. Interfaces between the fibrous and tapered nanostructures were observed by SEM, as shown in Figure 12 (a) and (b).

TEM and Selected Area Diffraction Results and Micro-Raman Results

TEM analysis indicated that the fibrous nanostructures observed in the surface plane had hollow cores and micron-scale lengths, as shown in Figures 13 (a)-(c). Selected area diffraction (SAD) patterns of these nanostructures revealed spot splitting of about 30°, consistent with that expected for nanotubes [50]. An example of a typical diffraction pattern is shown in Figure 14. Micro-Raman and SERS spectroscopies of the 5-hour sample also indicated the presence of well-graphitized carbon by relatively sharp peaks at

about 1580 cm^{-1} with 8-10 cm^{-1} full width half maximum (FWHM). A typical peak is shown in Figure 15.

TEM analysis of the tapered nanostructures is shown in Figure 16. The lengths of these nanostructures varied systematically as a function of reactor time. Approximate average lengths 0.4 microns, 0.5 microns, and 0.9 microns were observed for the 1-hour, 3-hour, and 5-hour samples. The average base width for the 1-hour and 3-hour samples was about 100 nm, while the average base width for the 5-hour sample was about 150 nm. Typical examples of the progressively etched silicon nanowires are shown in Figure 17.

Selected area diffraction (SAD), which included tilting to multiple zone axes, showed that these tapered structures were single crystal silicon nanostructures with the [100] orientation along the long axis. The orientation analysis is shown in Figure 18. The structures were tapered silicon nanowires, not hollow core silicon nanotubes.

TEM images revealed dark contrast dots of about 5-20 nm at the tips or along the sides of most of the tapered silicon nanowires, as shown in Figure 19. These dark contrast dots were subsequently shown by HR-TEM to be nanocrystalline iron.

High-Resolution TEM and EDS Results

HR-TEM was used to assess details of the silicon, carbon and iron nanostructures. Two size scales of fibrous carbon nanostructures were observed. Based on inner and outer diameters, these were identified as multi-wall CNTs and vapor grown carbon nanofibers,

as shown in Figure 20. Background from the carbon holey film limited further resolution of the wall structures. The dark contrast dots were shown by HR-TEM to be crystalline with well-defined atomic spacings consistent with bcc iron. EDS spectra provided further confirmation that these dark contrast features contained predominantly iron. The HR-TEM and EDS results are shown in Figures 21 (a)-(d). Iron nano-dots were sometimes observed at the tips of the carbon nanostructures as well as at the tips of the tapered silicon nanowires, also as shown in Figure 20.

Details of a heterojunction between a tapered silicon nanowire tip and a multi-wall CNT are shown in Figures 22 (a)-(c). The heterojunction appears to be about 4-6 nm wide. An EDS spectrum, shown in Figure 22 (b), provided further support for the identification of distinct silicon and carbon component parts.

Two types of nanostructures were observed in the plane of, and perpendicular to, the sample surfaces for 1 hour 0 minutes, 3 hours 10 minutes, and 5 hours 23 minutes reactor times. One was fibrous and micron-scale in length for all reactor times. The other was tapered, solid, and with an aspect ratio which changed as a function of reactor time. Analysis by TEM/SAD, HR-TEM/EDS, and micro-Raman/SERS indicated that the material compositions of these nanostructures were, respectively, carbon and silicon.

The carbon nanostructures were shown by TEM and HR-TEM to be multi-wall CNTs and hollow core vapor grown carbon nanofibers. The iron catalyst layer was shown by TEM and HR-TEM to be broken up into 10's of nanometer-sized droplets by the action

of the plasma. Iron dots with diameters between 5-20 nm were observed at the tips and along the sides of most of the tapered silicon nanowires. They were also observed at the ends of some of the CNTs and nanofibers. The observed multi-wall CNTs and carbon nanofibers would be consistent with growth via a Liquid-Metal-Solid growth mechanism in the presence of the iron catalyst droplets.

The silicon nanowires were shown by TEM and SAD to be solid tapered nano-wires, with the [100] orientation in the sample normal direction, and with progressive length variations as a function of reactor time. This results is consistent with formation by an etching mechanism of the (100) silicon substrate. Similar etchings of silicon [51-52] and other semiconductor materials [52-53] have been observed in argon-methane plasmas. However, in our experiments, the etching of the silicon nanostructures was simultaneously accompanied by LMS-mechanism growth of the carbon nanostructures. As the iron catalyst layer was broken up into 10's of nanometer-sized islands by the action of the plasma, it may have served as a nano-mask for the etching of silicon, as well as the LMS nucleation site for the growth of the multi-wall CNTs.

SEM images indicated that a nano-heterostructure junction was formed between the carbon nanostructures and the silicon nanowires at the pointed tips of the silicon. The formation of such junctions was observed for all three reactor times. The sample preparation method used in the present analysis reduced the probability of finding an intact heterojunction, but one intact specimen was located and analyzed by HR-TEM. The multi-wall CNT-silicon nanowire heterojunction appears to be about 4-6 nm wide,

which is a truly nanoscale heterojunction. Further experiments are needed to determine how many junctions had a similar structure, and if this type of connection is found within the macroscopic junctions observed by SEM.

The conditions for simultaneous LMS growth of multi-wall CNTs and etching of high aspect ratio silicon nanowires can be achieved in an Inductively Coupled Plasma reactor system. ICP reactors are the current state of the art in the semiconductor fabrication industry for large-scale silicon etching, due to high radial uniformity and low pressure/low temperature operating characteristics. Our results indicate that the incorporation of nano-materials produced by an LMS growth mechanism within a growth/etching fabrication cycle may also be possible. This may in turn lead to practical large-scale manufacturing of nano-components of multiple materials, using an existing reactor tool for both the conventional silicon and the new nano- electronic materials.

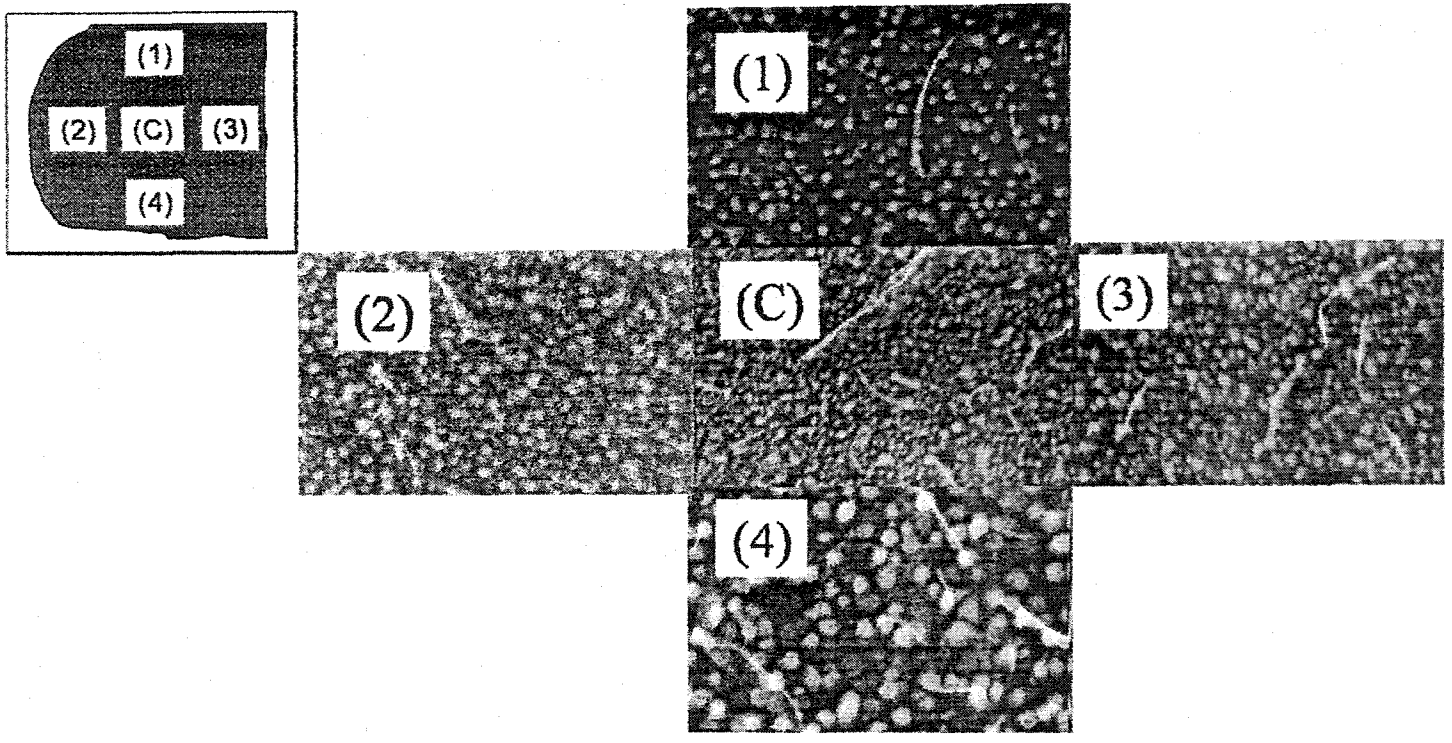

Figure 12: SEM Images Taken at 0° Tilt of Five Areas of Wafer on Which CNT-Si Nanowires Formed After Five Hours in ICP Plasma

SEM images taken at 0° tilt indicated a roughly uniform coverage of tubular nanostructures and "dots" for all samples. The above images are from the 5-hour sample

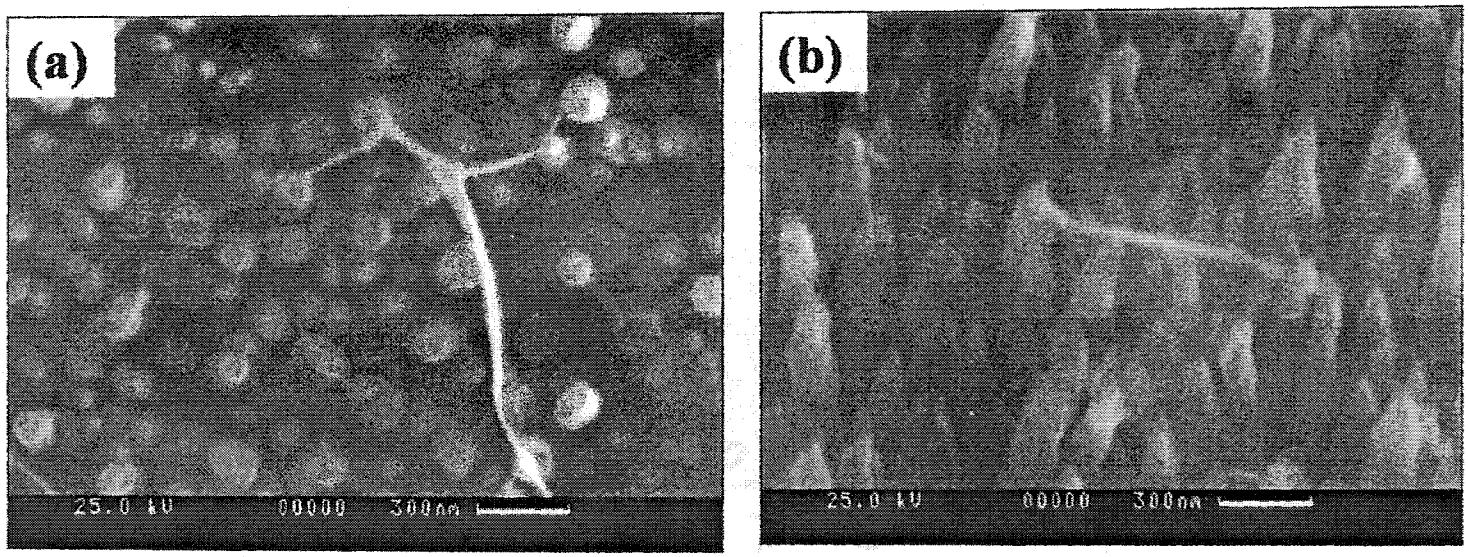

Figure 13: Close-Up SEMs OF CNT-Si Nanowire Heterostructures After 5 Hours
SEM images taken at (a) top view: 0° tilt and (b) side view: 40° tilt, indicate junctions between the fibrous and the tapered nanostructures

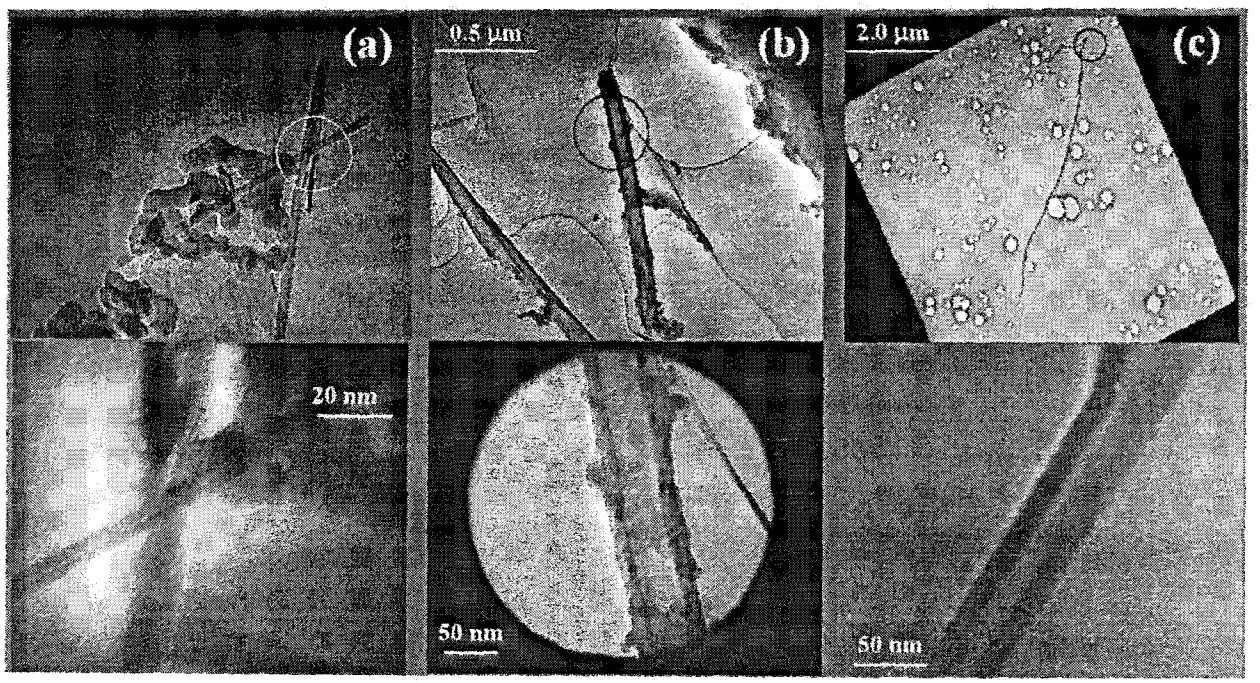

Figure 14: TEM Images of Carbon Structures Formed After 1, 3, and 5 Hours in ICP Plasma
TEM images of the fibrous nanostructures from the (a) 1-hour, (b) 3-hour and (c) 5-hour samples indicate approximately micron lengths and hollow core structures.

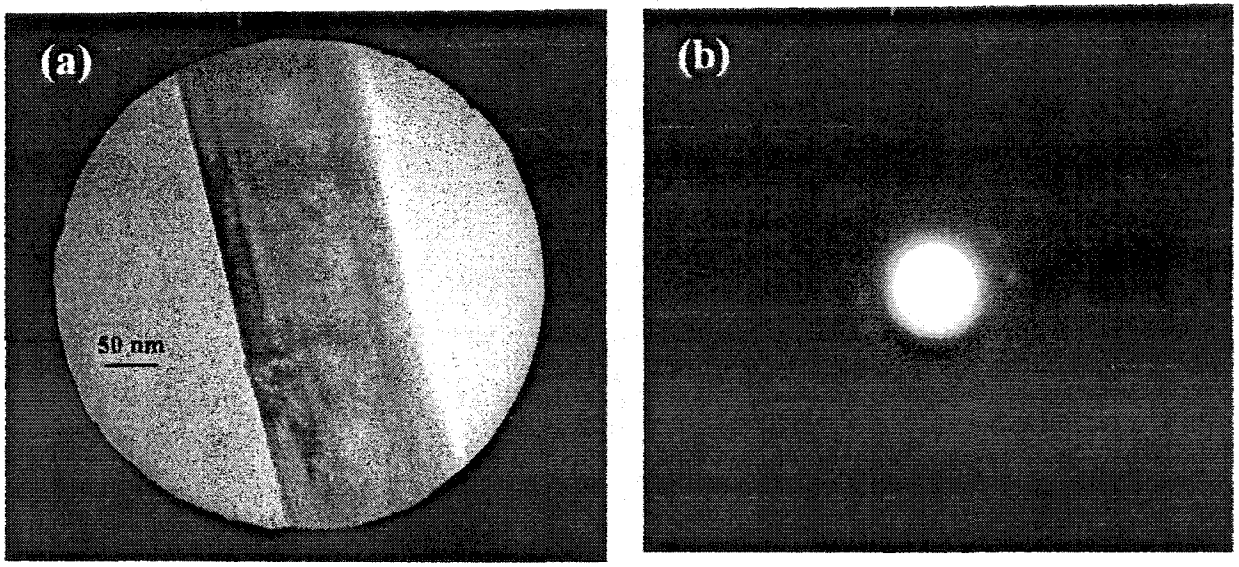

Figure 15: TEM mages and Corresponding Diffraction Pattern of a Carbon Nanotube Produced in ICP Plasma
(a) Bright field image with SAD aperture overlay and (b) rotationally correct SAD diffraction pattern showing spot splitting indicative of carbon nanotubes. Amorphous rings may be from either the tube surface structure or from the carbon support film

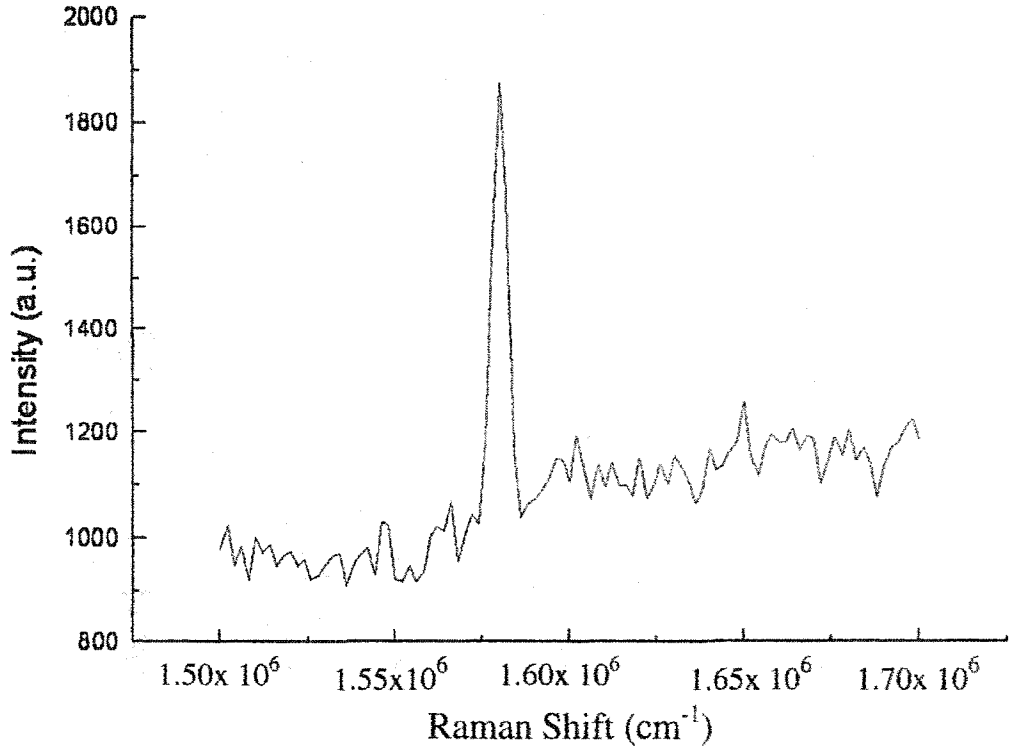

Figure 16: Micro-Raman Spectra From Wafer Placed in ICP Plasma for 5 Hours, Indicating Well-Graphitized Structures

Micro Raman and Surface Enhanced Micro Raman Spectroscopy (SERS) from the 5-hour sample indicate the formation of well graphitized carbon nanostructures by relatively sharp peaks with FWHM about 8-10 cm^{-1} at 1580 cm^{-1}.

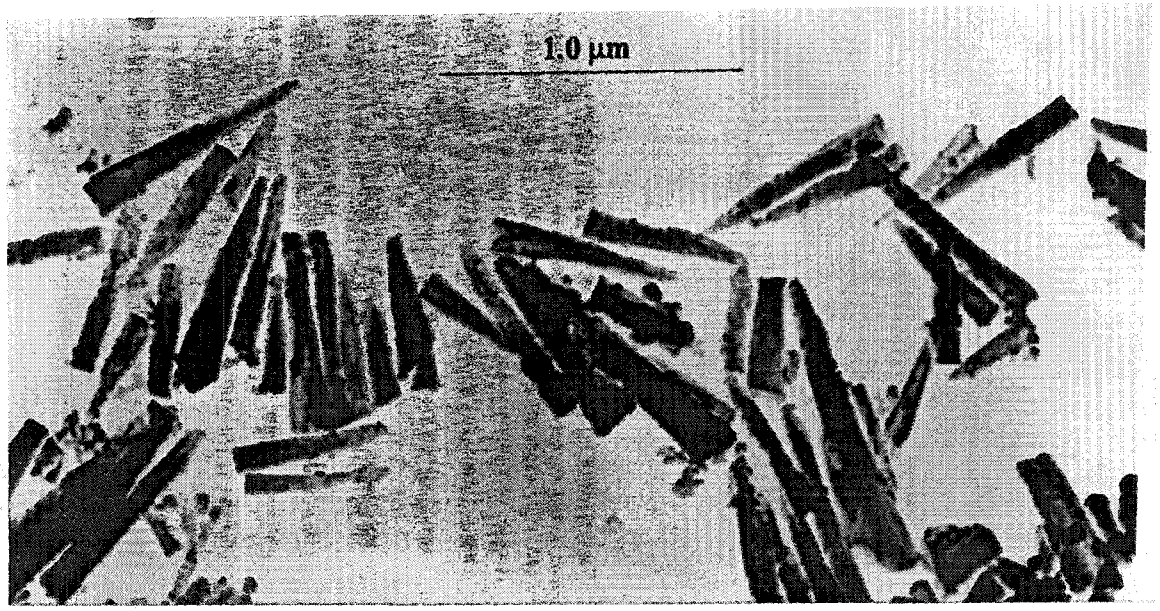

Figure 17: TEM images of the tapered silicon nanostructures
TEM images indicated the tapered structures were etched perpendicular to the surface. The above image is from the 5-hour sample.

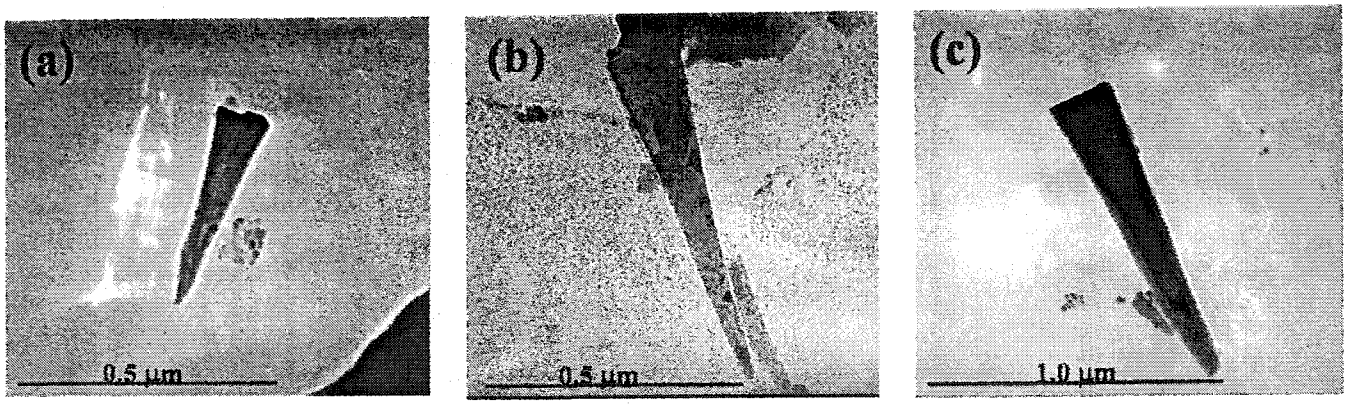

Figure 18: TEM Images Comparing Lengths and Base Widths of Silicon Nanostructures
TEM Images after appx. (a) 1 Hour (b) 2 Hours and (c) 5 Hours in ICP Plasma
TEM images indicate that the lengths of the tapered nanostructures varied progressively as a function of time: (a) 1-hour, (b)3-hour, and (c) 5-hour samples.

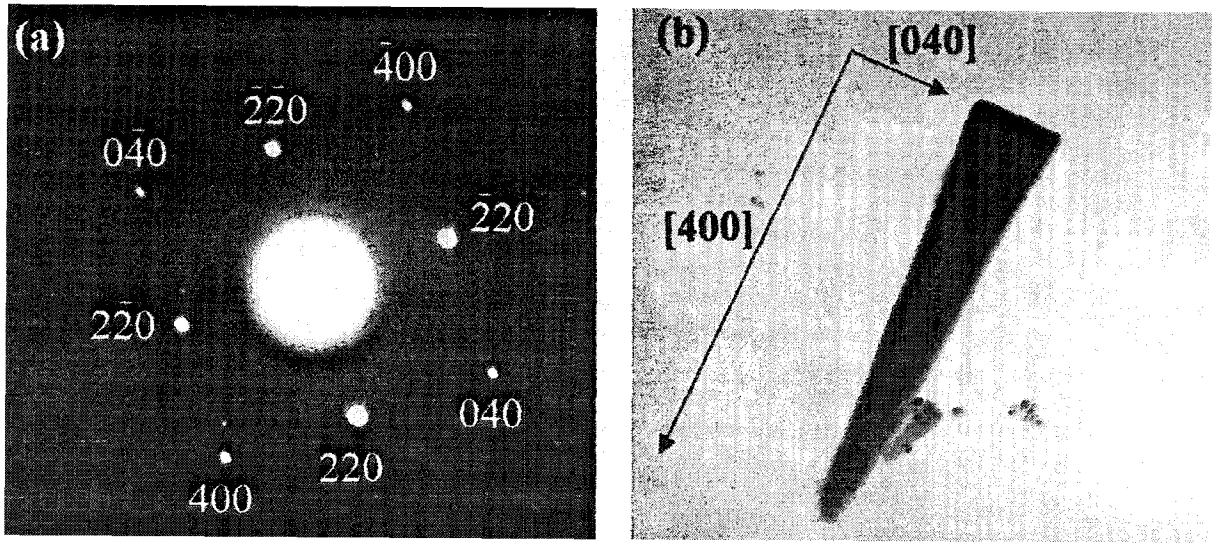

Figure 19: elected Area Diffraction Verified that the Nanostructures were Crystalline Silicon (From 5 Hour Sample)
SAD diffraction images from the tapered nanostructures show patterns indicative of single crystal silicon with the [100] orientation along the long axis.

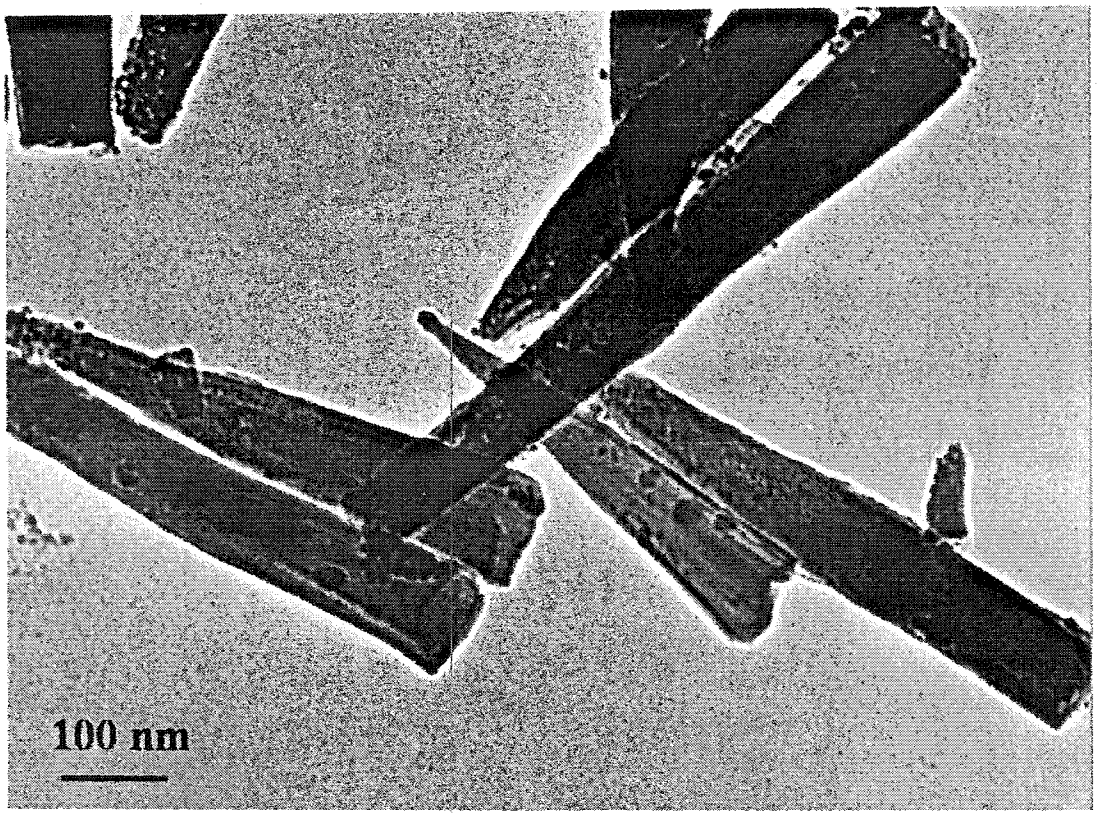

Figure 20: Verification of Identity of Dark Contrast Dots
Dark contrast dots at the tips and along the sides of the tapered silicon nanowires

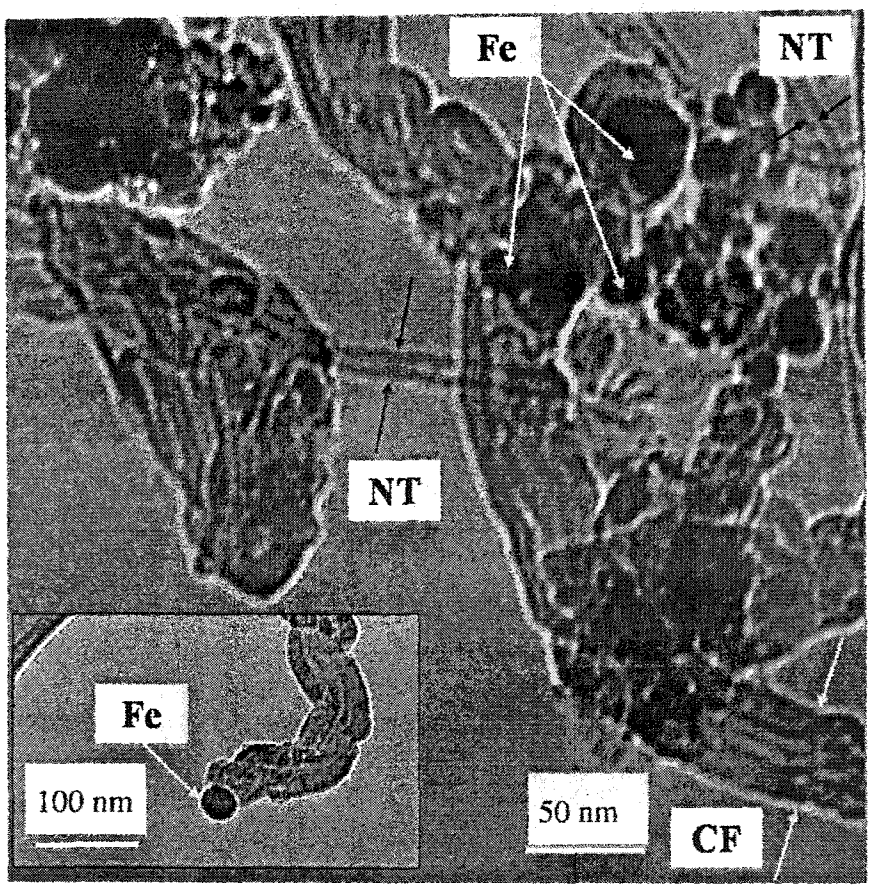

Figure 21: HR-TEM of CNTs and Carbon Fibers Produced after 5 Hours in Inductively Coupled Plasma
HR-TEM images indicate multi-wall carbon nanotubes (NT) and vapor grown carbon nanofibers (CF). Iron (Fe) dots were sometimes observed at the tips of the carbon nanostructures as shown in the lower left corner insert.

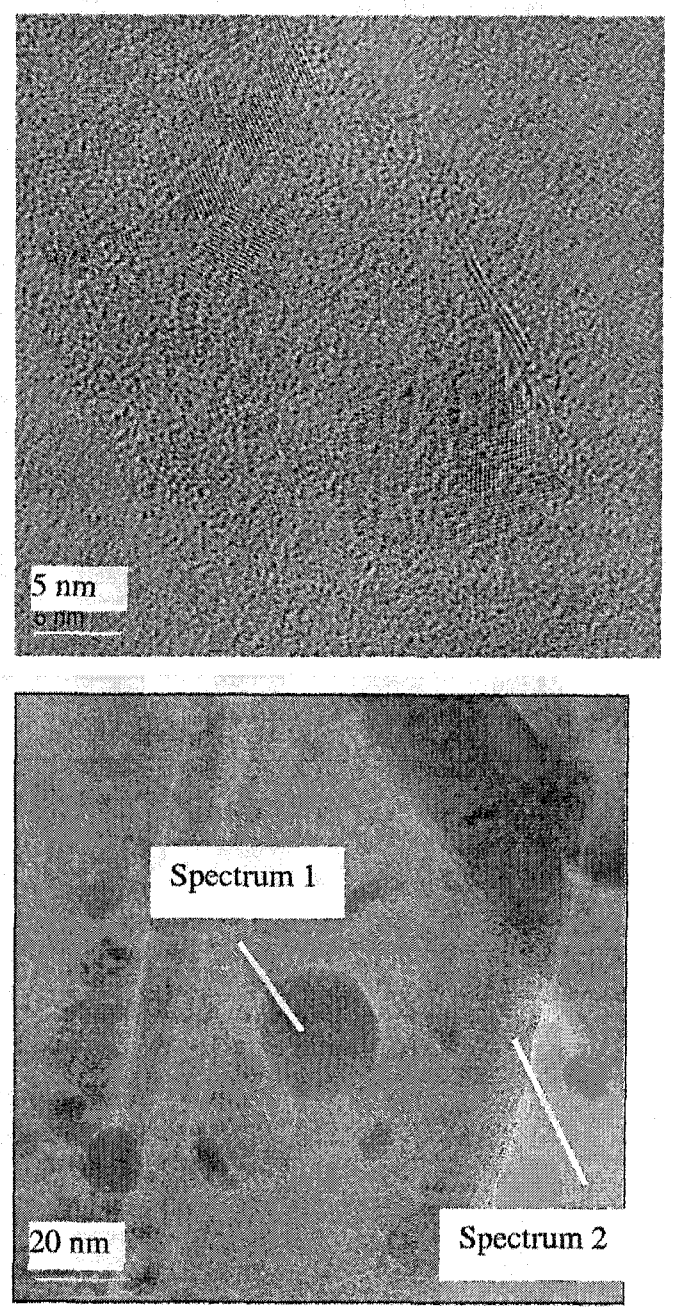

Figure 22 (a)-(b): HR-TEM Images of Silicon Components of CNT-Si nanowire Heterojunctions and Iron Nanodots
(a) The dark contrast dots showed atomic spacings consistent with nanocrystalline iron. (b) EDS spectra were used to further confirm the identification of the iron nanodots (Spectrum 1) on the silicon nanowires (Spectrum 2).

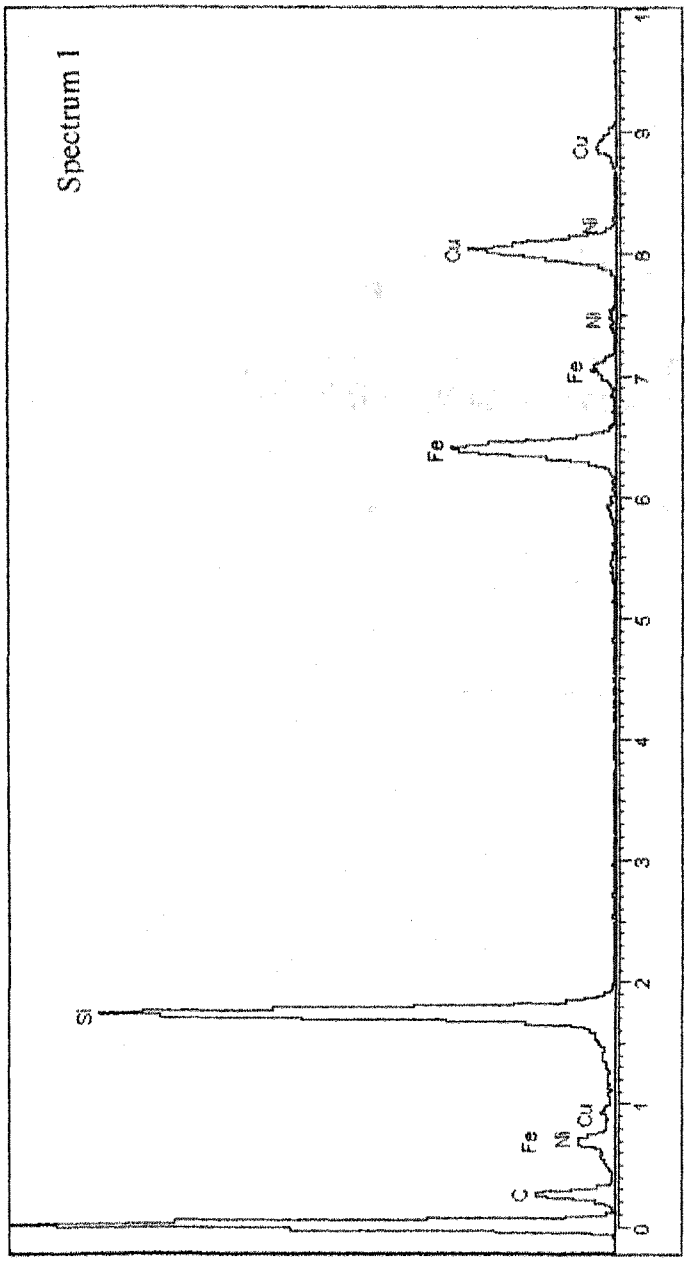

Figure 22 (c): EDS Spectrum of Iron Nanodots
EDS was used to further confirm the identification of the iron nanodots (Spectrum 1)

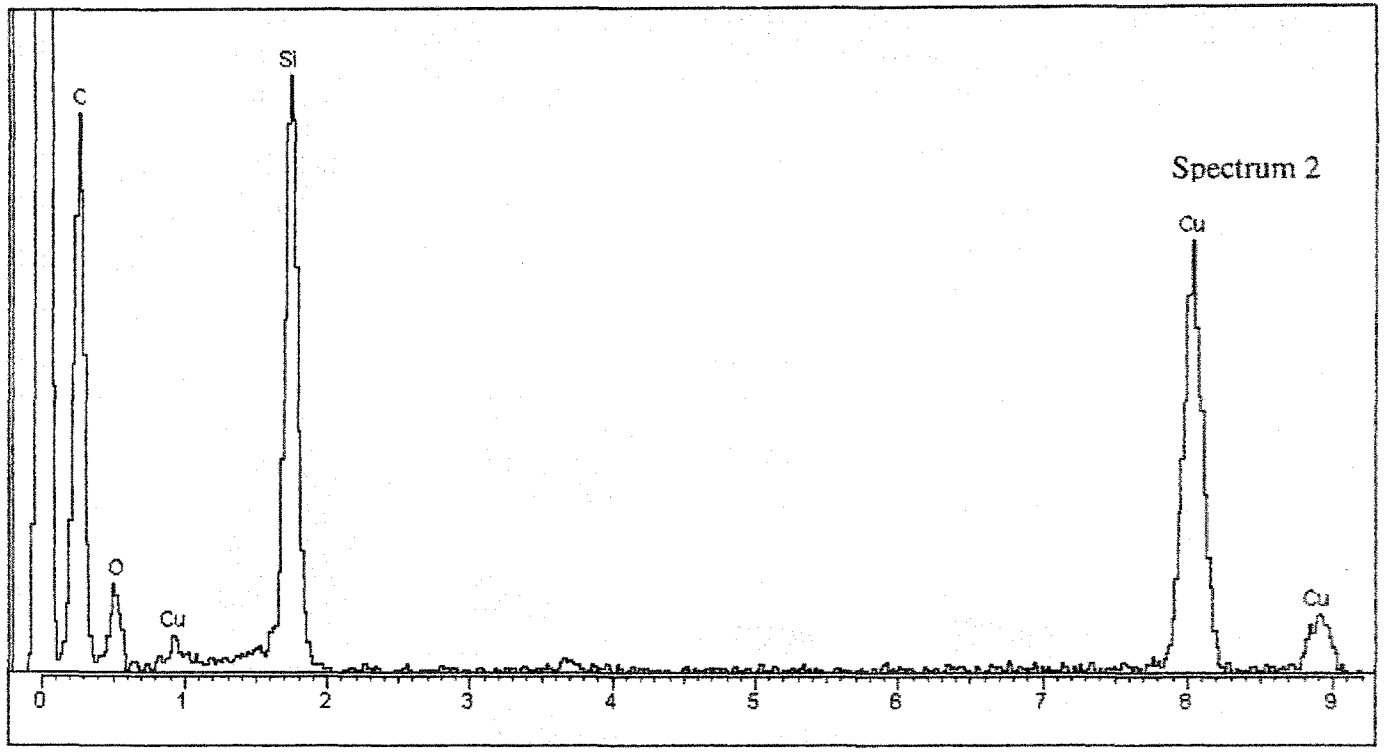

Figure 22 (d): EDS Spectrum of Silicon Nanowires
EDS was used to further confirm the identification of the silicon nanowires (Spectrum 2).

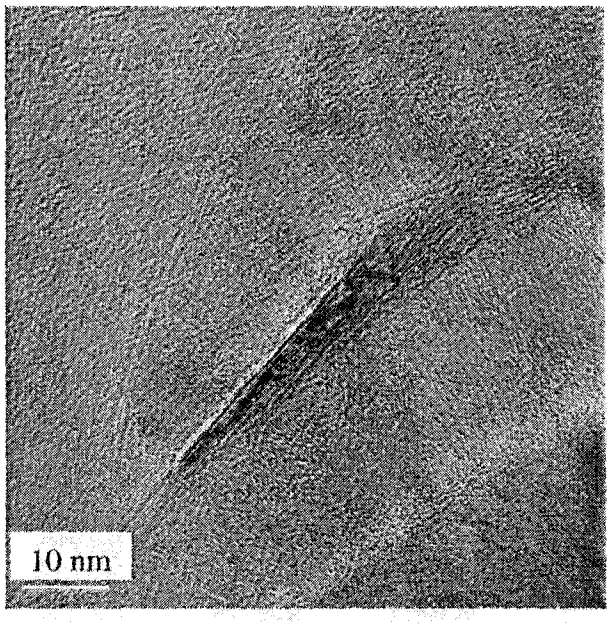

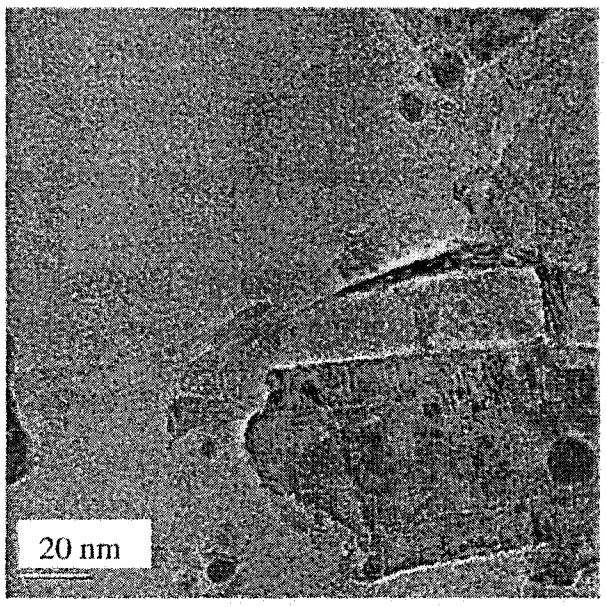

Figure 23 (a)–(b): HR-TEM IMAGES an Intact CNT-Si-Nanowire Heterojunction (a) HR-TEM image of a heterojunction between a MWCNT and a tapered silicon nanowire tip (b) Lower magnification view of the MWCNT-silicon nanowire heterojunction.

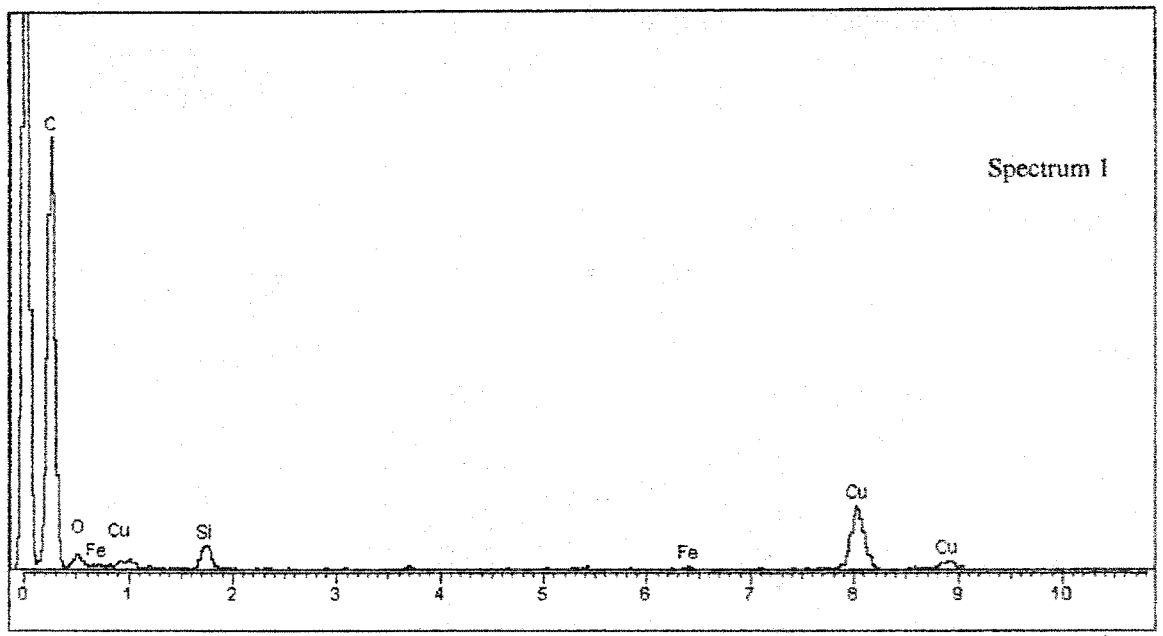

Figure 23 (c): EDS Spectrum of an Intact CNT-Si-Nanowire Heterojunction
EDS was used to support the silicon identification

CHAPTER 5

HEAVY-ION INTERACTIONS IN NEW NANOSCALE MATERIALS

Introduction

To reiterate, space exploration is entering a new era, with the advent of new micro space probes, and the increasing use of miniaturized equipment. The United States space agency, NASA, is planning to deploy in space electronic devices and enhanced composites constructed from the newly developed nanotube and nanowire components [55]. Heavy ion irradiation is a significant component of the Low Earth Orbit (LEO) space radiation environment, where an increasing number of space platforms and satellites will operate. Heavy ions are known to induce failures in current state of the art components and electronic devices, through uncontrolled ion implantation, which alters the channel conductance [56], and through lattice disruption mechanisms [57-58]. These problems may be exacerbated in microprobes, which have less radiation shielding. In addition, state of the art conventional transistors are increasingly sub-micron in dimension and more susceptible to radiation damage.

Experimental Procedure

The radiation experiments were performed at the National Superconducting Cyclotron Laboratory (NSCL) at Michigan State University, whose available beam energies well match the energy spectra of abundant charged particles in space radiation environments. To simulate radiation doses from high-Z ions, the samples were irradiated using the Krypton-86 standard primary beam at 142A MeV/nucleon. As there are no published

guidelines for beam exposure times in nanoscale materials, these experiments were conducted with doses and exposure times comparable to those that can be expected to damage or destroy current state-of-the art silicon circuits. Failures under dose in a diverse range of silicon devices and technologies indicate that initial damage thresholds are at about 10 Gy [58]. Thresholds for radiation-hardened devices are at about 1000 Gy. Almost all devices will fail before doses reach 10^5 Gy.

Single wall CNTs (SW-CNT), multi-wall CNTs (MW-CNT), tapered silicon nanowires (T-SiNW), electrospun carbon nanofibers (ES-CNF), and vapor-grown graphitic carbon fibers (VG-CF) were irradiated. The choice of samples allowed us to investigate heavy ion interactions with multiple carbon wall structures: graphene single crystal, *i.e.*, SW-CNT, nested graphene single crystal, *i.e.*, MW-CNT, highly ordered organic networks, *i.e.*, ES-CNF, and stacked graphite crystal platelets, *i.e.*, VG-CF. Investigation of the silicon nanowires will allow comparisons between the behaviors of carbon versus silicon at the nanoscale. The SWCNTs were in the form of a buckypaper to maximize the volume available for heavy-ion interaction.

Sample Preparation

The NASA CNTs and the "Tubes@Rice" were ultra-sonicated in ethanol, placed in quartz capillary tubes and the ethanol was then allowed to evaporate, leaving the samples (except the carbon nanofibers and the CNT-Si nanowire heterostructures on the walls of the tube. In the case of the CNT-Si nanowire heterostructures, the wafers on which they were grown were simply placed in the quartz tubes after being cleaved to a size that

allowed them to fit into the tubes. The electro-spun carbon nanofibers were placed in the tubes in their original form.

100 Gy, 1,000 Gy and 10,000 Gy were set as the target doses for our experiments. The individual doses varied somewhat as a function of mass, sample type (density), and packing volume. Fifteen samples were placed in quartz tubes arranged as 6/5 tubes per row wide (close packing) and 2 rows deep in a rectangular holder. Each individual quartz tube had an outer diameter of 3 mm, an inner diameter of 2 mm, and a total length of 70 mm, of which about 20 mm at the top, containing the samples, was exposed to the beam. The quartz tube array was placed in front of the beam port. Dose calculations included the effects of the quartz sidewalls in the first and second rows, the zirconium foil vacuum window and the small air gap between the window and the sample array. The beam was transported to the NSCL N4 vault end station by dipole and quadrupole magnets, and focused there to an area having dimensions of 2-cm (height) by 2-cm (width), as measured from known dimensional markings on the beam-viewing scintillator placed at the beam line exit vacuum window. The beam area was sufficient to irradiate the complete extent of the samples. The upstream current was measured in the extraction channel of the K1200 cyclotron, using a remotely operated beam probe. The exit and upstream current measurements were ratioed to access the beam factor. For each subsequent experiment, the upstream current was measured both before and after the run. From the Faraday cup measurement and subsequent probe measurements, a stable current of 0.3 particle-picoamperes (ppA) or 1.87×10^6 particles per second, was estimated as the

beam current at the exit point during the experiments. Therefore, the particle flux was 4.68×10^3 particles per second per mm^2.

Pre-Irradiation Calculations

Prior to the irradiation of the samples, calculations were performed to estimate the irradiation times necessary to achieve the desired doses of 100, 1,000, and 10,000 Gys First, the necessary dose was determined. This was done as follows:

1) The mass of the carbon was calculated. The density of the carbon was estimated by the value for graphitic carbon, 2.24 g/cm^3. The density was then multiplied by estimated volume of the carbon, 2.84 E-02 cm^3 (R=thickness=.05 cm, height=1 cm).
2) The energy loss was determined after a series of calculations using a specially developed software package at the NSCL. Hence, the dose per part Gy/ion, which is the energy loss in the carbon divided by the mass of the carbon determined to be 7.35 E+06 per part Gy/ion

Secondly, the total number of ions needed to achieve the desired doses was determined by dividing the desired doses by the dose per part Gy/ion. This gave the total number of ions needed to achieve 100, 1,000 and 10,000 Gy. Finally, to determine the necessary amount of time needed to achieve the doses, the total number of ions necessary to achieve the desired doses was divided by the beam current, which was .3 particle pico Amps (ppA) =1.8 E+06 particles per second

The results are tabulated below in Table 1

Table 1. Calculations Performed to Determine Irradiation Times

86 Kr	Dose per part Gy/ion	Dose (Gy)	Ions/sec	Time at .3 ppA (Sec)	(Min)	(Hr)
142 MeV	7.35 E-06	100	1.36 E+07	1.13 E +00	1.89 E-02	3.15 E-04
		1,000	1.36 E+08	1.13 E +00	1.89 E-01	3.15 E-03
		10,000	1.36 E+09	1.13 E +00	1.89 E+00	3.15 E-02

Post-Irradiation Calculations

Detailed calculations were made in order to verify the exact dose that the single wall CNT film was exposed to, seen in Table 2. The approximate area of the carbon film was calculated and was carefully weighed. The parts per second were then calculated to determine how many ions were reaching the sample and the required time in order to achieve the desired dose.

Table 2. Calculations Performed to Determine Actual Doses.

Sample	~Carbon Area (mm^2)	Sample Mass (g)	Ions	Time (sec)	Sample Dose (Gy)
1	16.92	0.013	7.92E+04	900	3.42E+02
2	16.92	0.005	7.92E+04	90	8.89E+01
3	16.92	0.0099	7.92E+04	15	7.49E+00

Radiation Experiment Results

Pre versus post irradiated specimens were investigated for structural and chemical alterations. SEM, FE SEM and AFM were used to investigate changes to the external structure. Transmission electron microscopy and high-resolution transmission electron microscopy were used to investigate changes in the internal structure. Selected area

diffraction was used to detect any departure from crystallinity. Micro Raman spectroscopy/Surface enhanced Raman Spectroscopy and was used to investigate the molecular bonding present and to monitor the appearance of any defect induced peaks.

The results are presented in *decreasing* order of damage effects, to show the damage mechanisms present in the VGCF and ESCNF samples under heavy ion irradiation, and their absence in the irradiated SWCNT and MWCNT samples.

Radiation Damage Effects in the VGCF Samples

Pre-irradiation characterization of the VG-CF was obtained by SEM, TEM and micro Raman spectroscopy and indicated well graphitized hollow core stacked platelet [56] fibers with fairly uniform 150 nm diameters of about 150-200 nm, as shown in Figure 23(a). By 90 seconds (1,000 Gy) irradiation, substantial damage was observed over most of the sample area, as shown in Figure 23 (b). The fibers become vaporized into disordered or amorphous carbon with very few fibers remaining.

Sample damage was so severe that insufficient amounts of the 15 and 900 second samples remained for analysis, after extraction from the quartz tubes. In the future, a different sample preparation technique using thin flat quartz plates will be employed. Also, it will be known in advance that this type of sample can be reduced to a very fine powder which is very difficult to handle. Figure 24 shows a possible damage mechanism associated with this type of radiation damage. The radiation beam introduces an interstitial, an excited 86Kr ion, which induces a vacancy in the plane of the graphite.

This interstitial also creates a vacancy in the graphite. There is then a subsequent contraction in the in-plane (a-plane) direction and expansion in the out of plane (c-plane) direction, resulting in the disintegration of the fiber.

Radiation Damage Effects in the ESCNF Samples

The electrospun carbon nanofibers (ES CNF) produced at Michigan State University using a homebuilt system used poly ε-caprolactone as the polymer monomer; the ES CNF fibers produced at the Donaldson company (industrial partner of Professor Melvin S. Schindler) used a propriety mixture. Tapping Mode Atomic Force Microscopy of the post-irradiation electrospun carbon nanofibers indicated damage spots (10's of nms), which may be due to intense local heating which caused "melting". FE SEMs, shown in Figure 32, were used to confirm that the results of the AFM analyses were truly representative.

TEM analysis also showed progressive damage with increasing radiation, as shown in Figure 35. We noticed the appearance of dark contrast areas, which seemed to be increasingly prominent by 900 sec. Dark contrast areas may indicate changes in molecular structure, corroborating the hypothesis that local "melting" did occur.

This interpretation would be consistent with a known radiation damage mechanism in polymer materials [65]. Intense heating could be caused by scission of the side chains or by transfer of phonons down a carbon chain until an end site is reached. Further damage could have been generated through formation and release of volatile oxygen compounds

such as CO and CO_2. The nature and degree of cross-linking and hence the availability of side chains as a function of tube diameter is currently under investigation, and will be investigated in a further series of radiation experiments.

Radiation Results for the SWCNT Samples

A continuous film of single wall CNTs (bucky paper) was studied to maximize the possibility of an interaction. The following results are shown in Figures 27 (a)-(b). Tapping Mode Atomic Force Microscopy studies of the surface morphology did not indicate any obvious damage at any radiation dose. Wide area analysis by FE SEM (20 microns x 20 microns) also did not indicate any obvious morphological changes.

Micro-Raman is a volumetric measure over an even wider area. For our Raman system the 60x objective used in these experiments, and the spot size was 30 microns in diameter. The Micro-Raman spectroscopy of the tangential mode region, 1500-1700 cm^{-1}, clearly indicated the double peak at about 1560 and 1590 cm^{-1}, that corresponds to the well-studied signature of mixed metallic and semiconducting single wall CNTs [14]. In the 900 second (10,000 Gy) Raman spectrum, a slight peak at about 1350 cm^{-1} may indicate the presence of some disordered carbon. The conclusion was the SWCNTs did not show any obvious radiation damage, when investigate by AFM, FE SEM, and Micro-Raman Spectroscopy

Radiation Results for the MWCNT Samples

FE SEMs of the multi-wall carbon nanotubes also showed consistent radiation resiliency throughout all radiation doses. In the pre irradiated sample, the nanotubes were difficult to find and seemed to be buried in the disordered carbon bulk. The MWCNT show with increasing cleanness in the 15 sec, 90 sec and 900 sec FE SEM image. It is possible that the heavy ion irradiation vaporized some of the amorphous carbon content of the samples, leaving the MWCNT intact and exposed.

One sample of the Multi wall CNTs was studied via High-Resolution transmission electron microscopy. The 90 second (1,000 Gy) irradiated sample was showed no visible structural damage as seen in Figure 26. Further HR TEM of all of the irradiated MWCNT samples is ongoing, and further Micro Raman spectroscopy is also ongoing.

Summary of Heavy Ion Irradiation Results

Morphological and molecular bonding characterizations of single wall buckypaper CNT films and multi-wall CNT samples indicated little damage for 100, 1,000 and 10,000 Gy 86-Krypton radiation doses at 142 AMeV/nucleon. By comparison, vapor grown carbon fibers showed substantial disruption after 90 seconds heavy ion irradiation (1,000 Gy), and total loss by 900 seconds. Electrospun carbon nanofibers showed damage at all radiation doses, with increasing damage at increasing doses, and extensive damage by 900 seconds. The damage pattern for electrospun carbon nanofibers appears to be different than that for vapor grown carbon fibers. Known damage radiation mechanisms for graphitic vs. polymeric materials are consistent with the observed results for vapor

grown carbon fibers and electrospun carbon nanofibers. However: neither damage mechanism was explicitly observed in irradiated single and multi-wall carbon nanotubes.

These results indicate that CNT textiles and components may have good heavy ion radiation resilience that would make them appropriate for deployment in space applications.

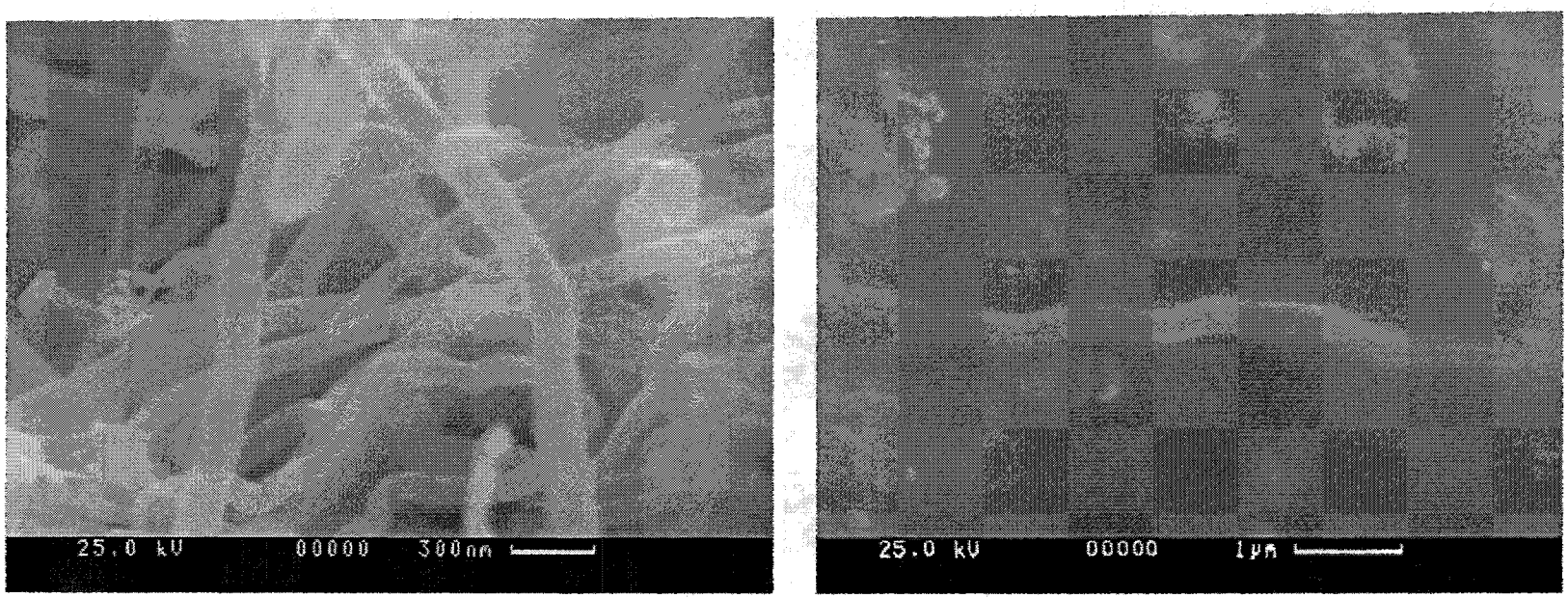

(a) (b)

Figure 24: SEM Images of Vapor Grown Carbon Fibers
The pre-irradiation fiber diameter is about 150 nm. SEM of (a) Pre-irradiation (b) radiation damage at 90 seconds

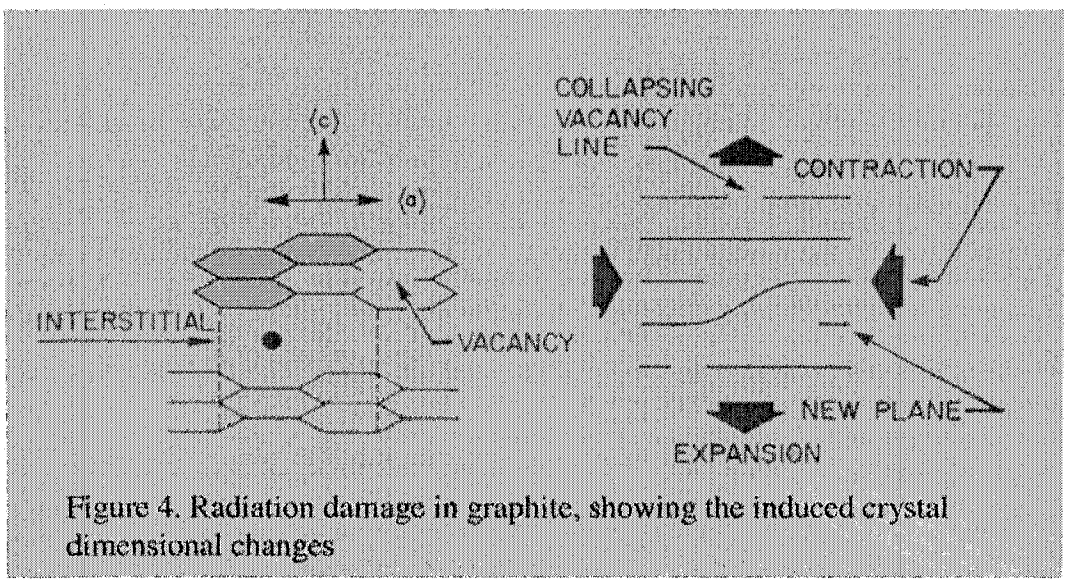

Figure 4. Radiation damage in graphite, showing the induced crystal dimensional changes

Figure 25: Damage Mechanisms in graphite due to radiation (Taken from [66]: T.D. Burchell, "Radiation Effects in Graphite and Carbon-Based Materials", MRS Bulletin Special Issue: Materials Performance in a Radiation Environment, Vol. 22, pp. 29-35 (1997))

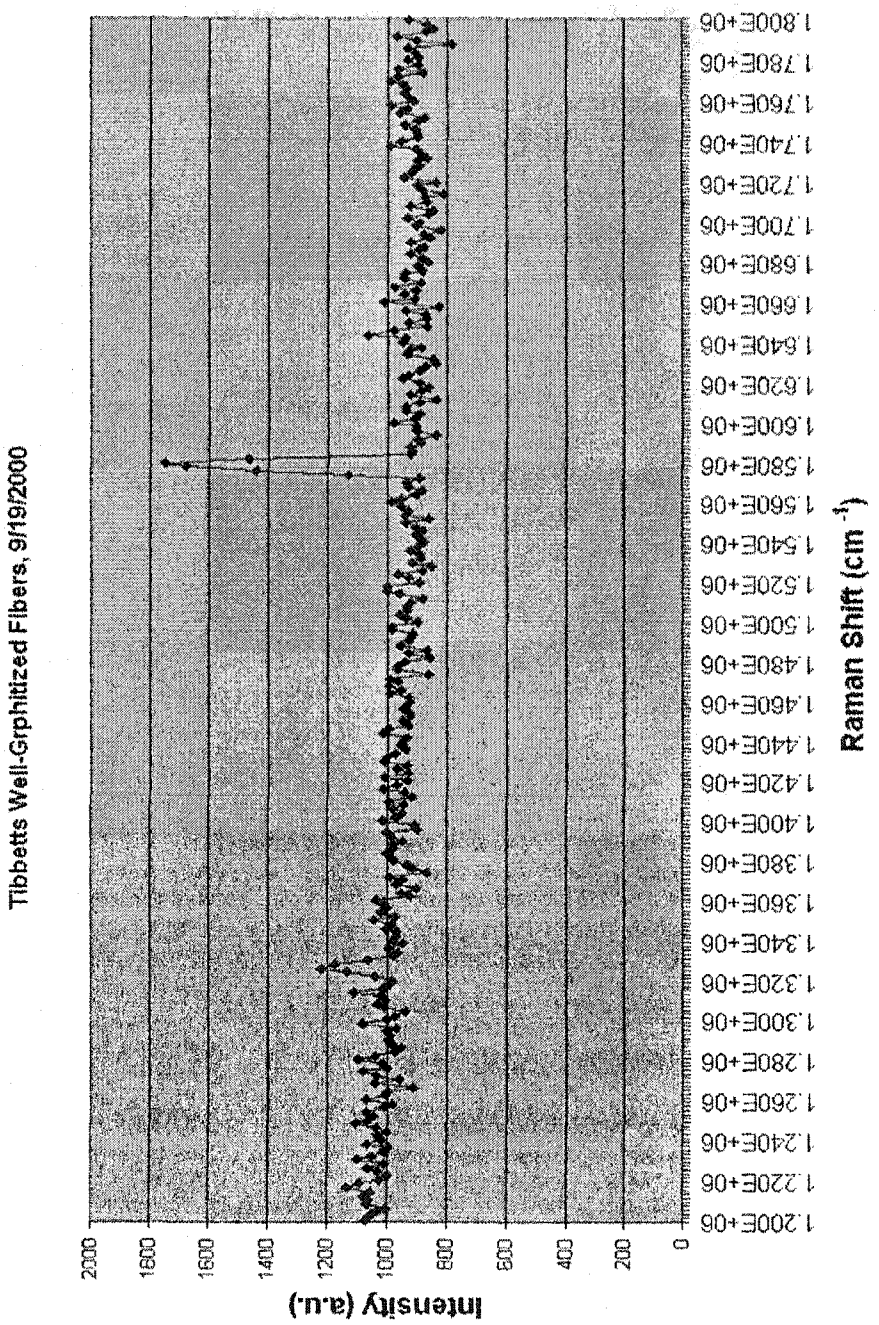

Figure 26: Raman Spectra of well-graphitized fibers prior to irradiation showing a strong peak at 1580 cm-1

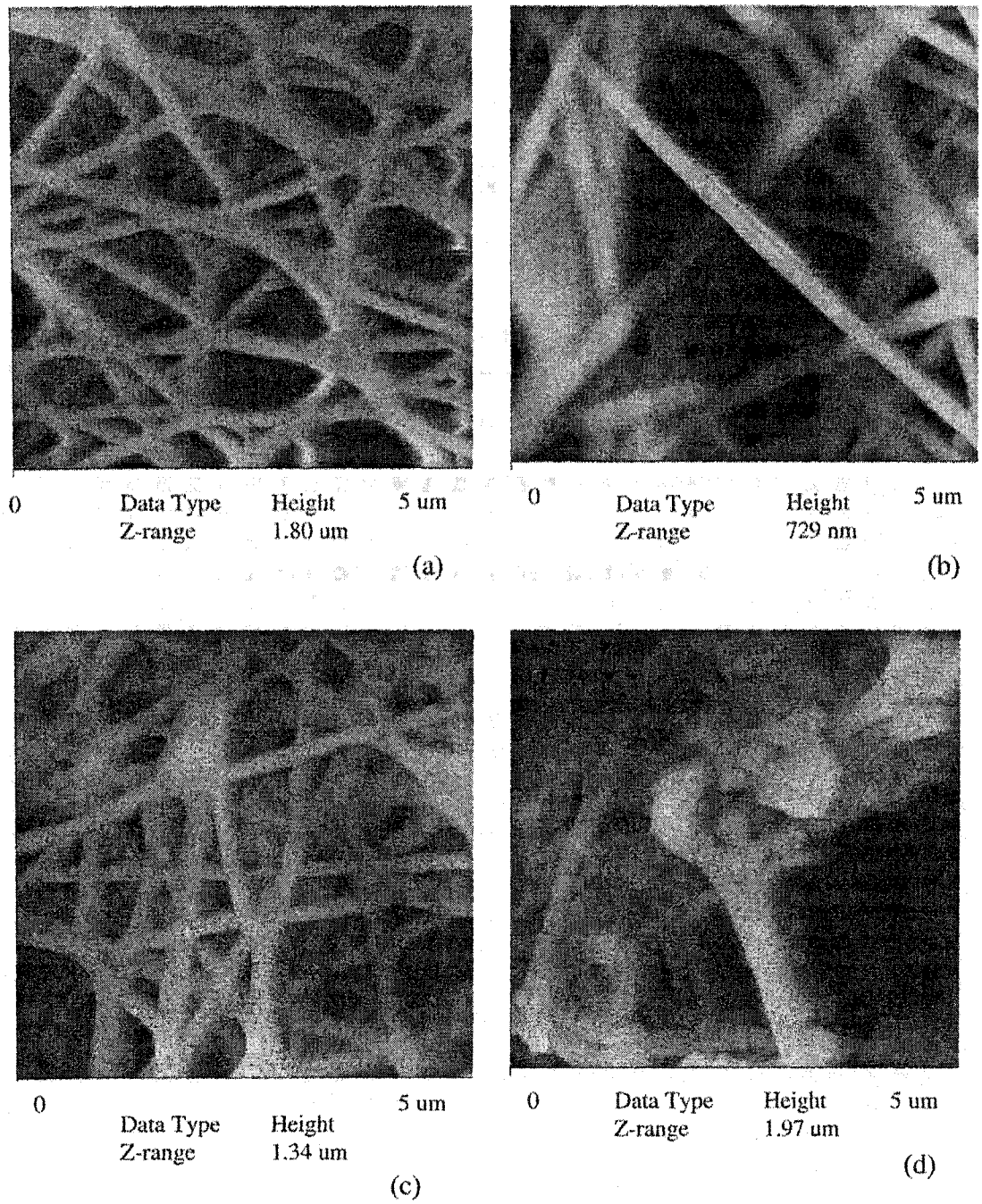

Figure 27: AFM Height Images of Electrospun Carbon Nanofibers Electrospun carbon nanofibers (precursor monomer poly(ε-caprolactone)). The diameter is about 200 nm. Tapping Mode AFM of (a) pre-irradiation (b) radiation damage at 15 seconds (100 Gray), (c) radiation damage at 90 seconds (1,000 Gray), (d) radiation damage at 900 seconds (10,000 Gray)

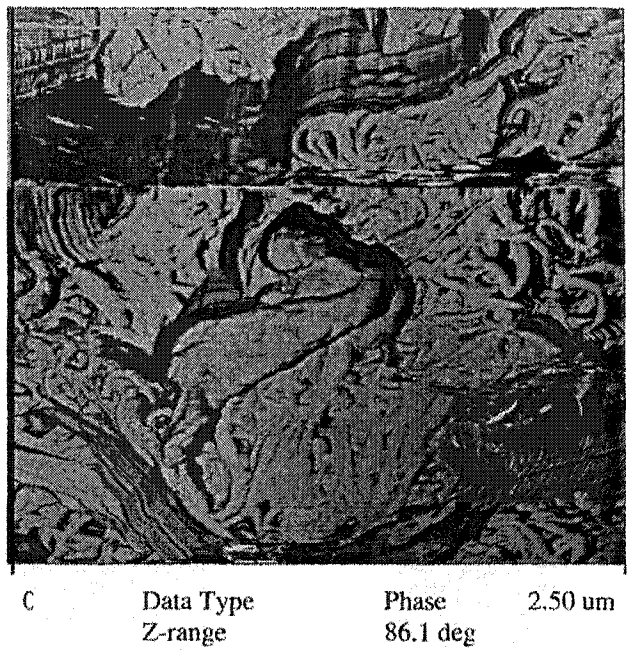

(a)

Figure 28 (a): AFM PHASE Image of Tubes@Rice Prior to Irradiation Continuous film of single-wall carbon nanotubes, individual diameter about 1.4 nm. Tapping Mode AFM images all resembled (a) indicating no observable morphological damage.

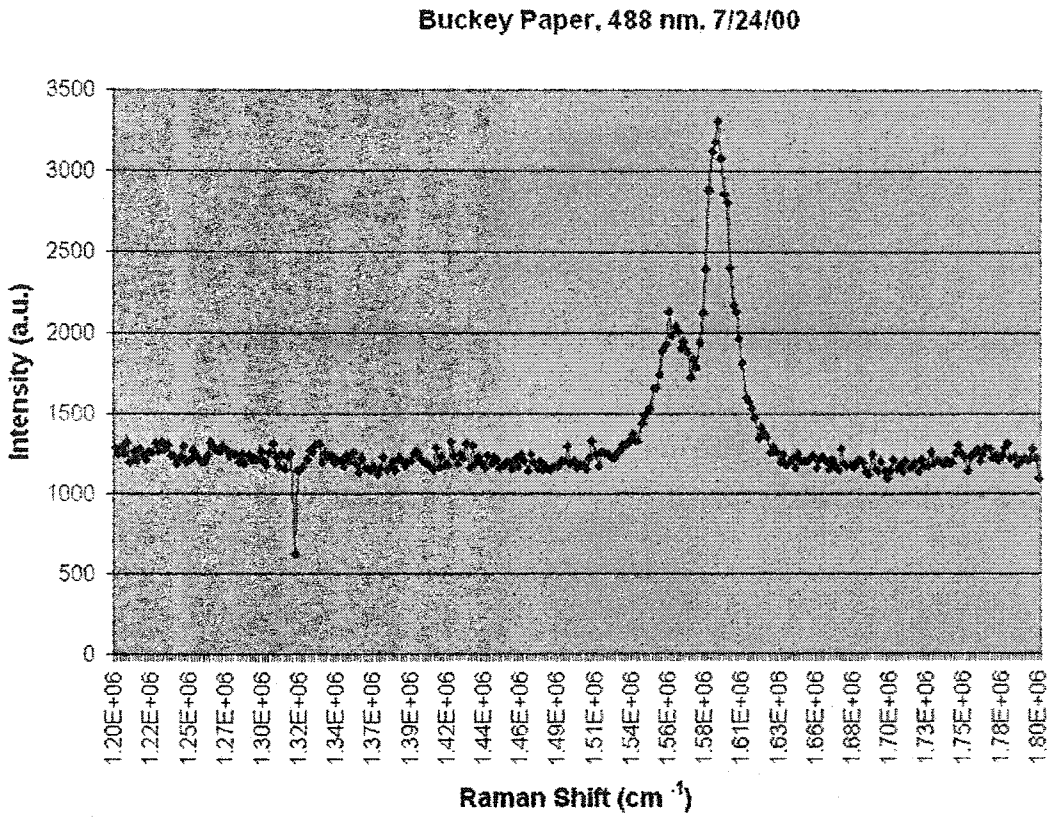

(b)

Figure 28 (b): RAMAN SPECTRA OF TUBES@RICE PRIOR TO IRRADIATION GRAY. Micro Raman spectroscopy of the pre-radiated sample

(c)

Figure 29: Raman Spectra of Tubes@Rice After a 900 seconds.
Micro Raman spectroscopy of irradiated sample after 900 seconds (340 Gy) also indicated little damage

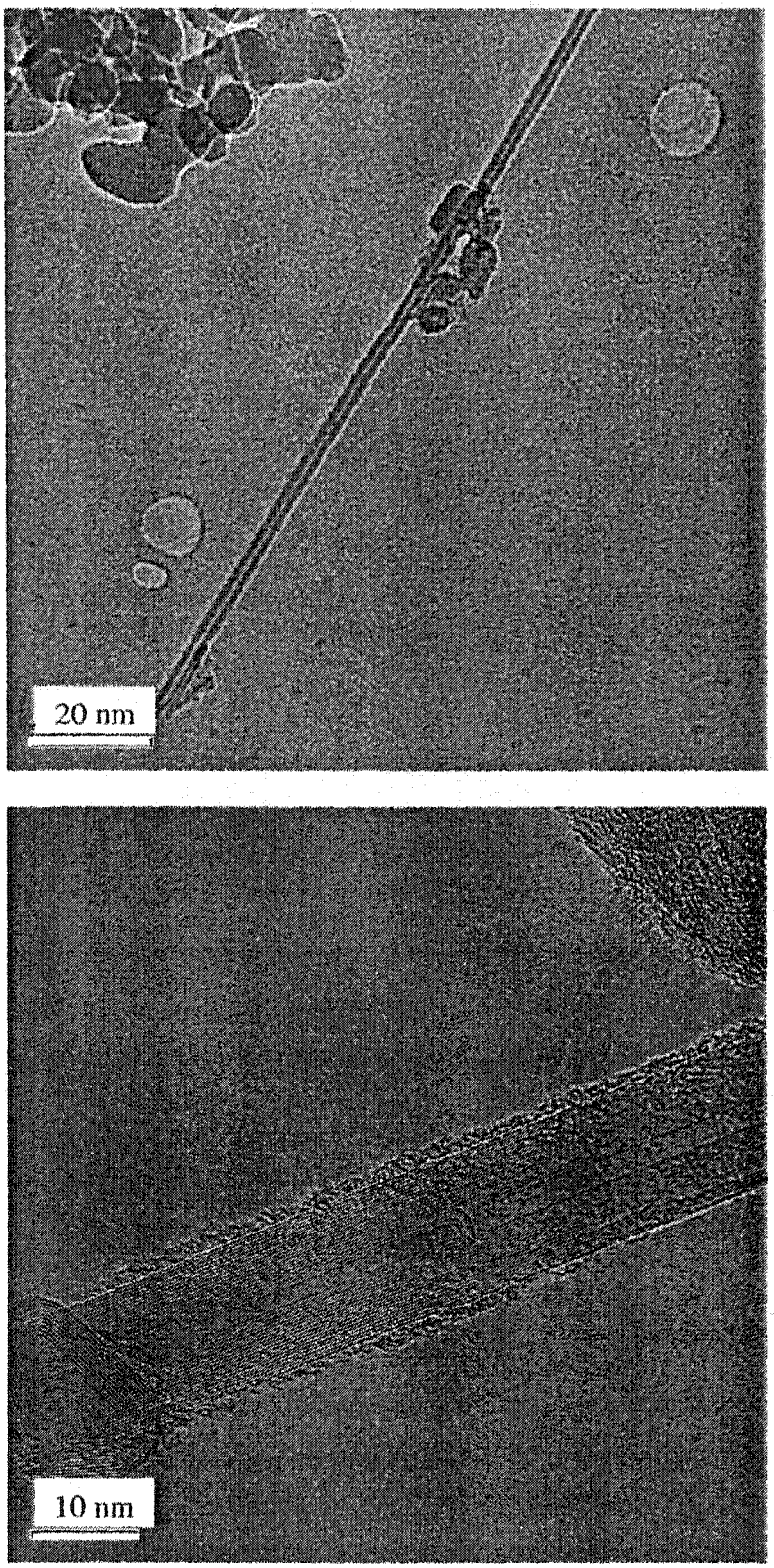

Figure 30: HR-TEM Images of Multi-wall CNTs after 90 seconds. Both images show no radiation damage after 90 seconds

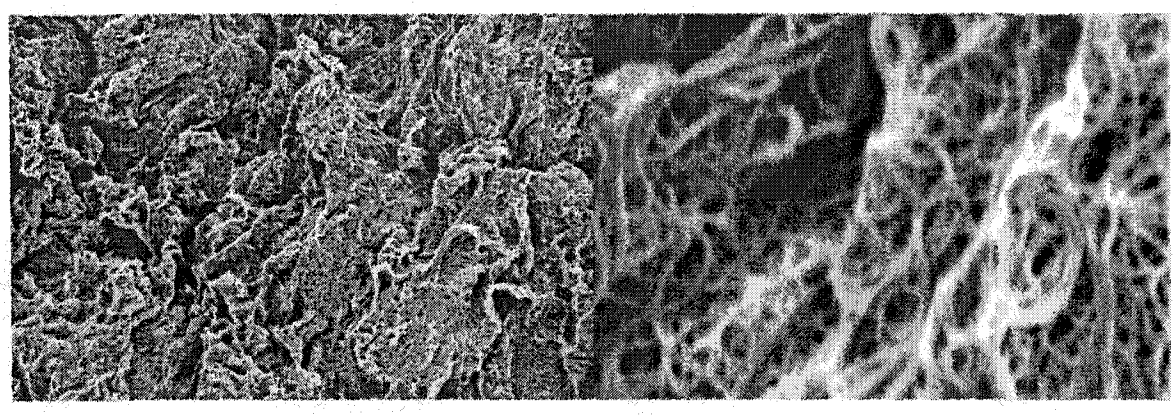

Figure 31: FE SEM Images of Tubes@Rice prior to irradiation.
[Images taken by Benjamin Jacobs]

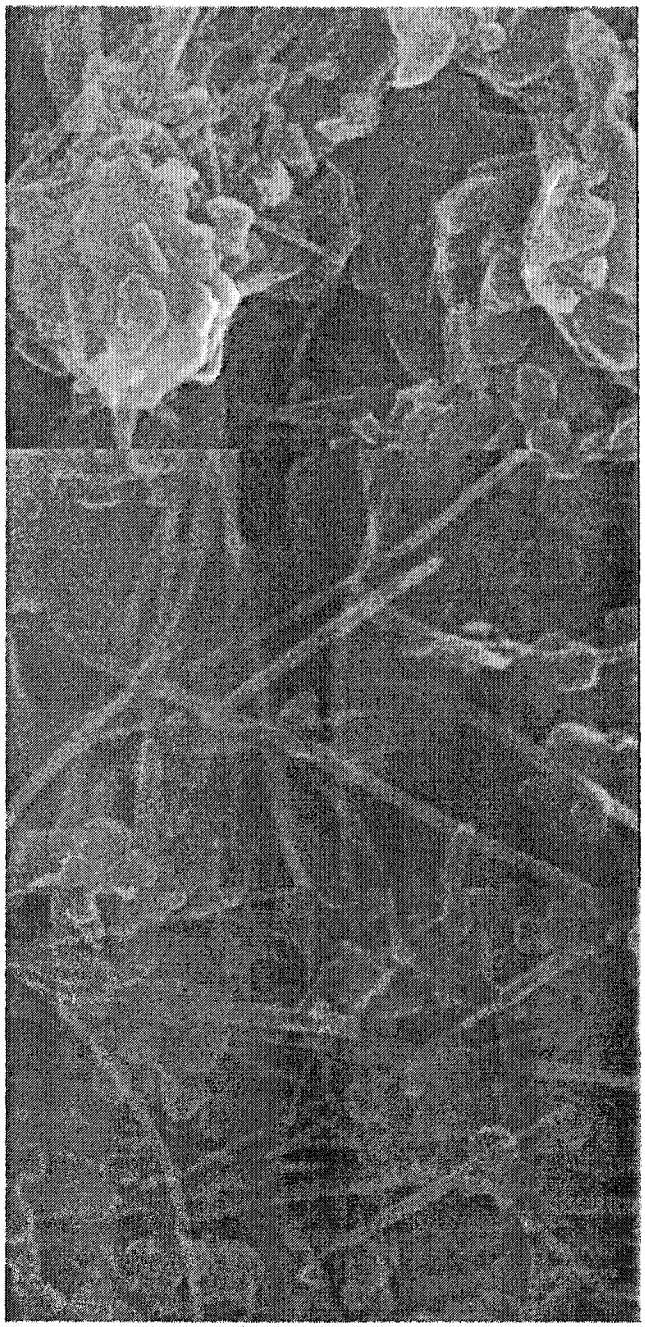

Figure 32: FE SEM Images of MWCNTs grown at the NASA Goddard Space Flight Center taken after irradiation.
a) 15 seconds b) 90 seconds and c) 900 seconds of irradiation
[Images taken by Benjamin Jacobs]

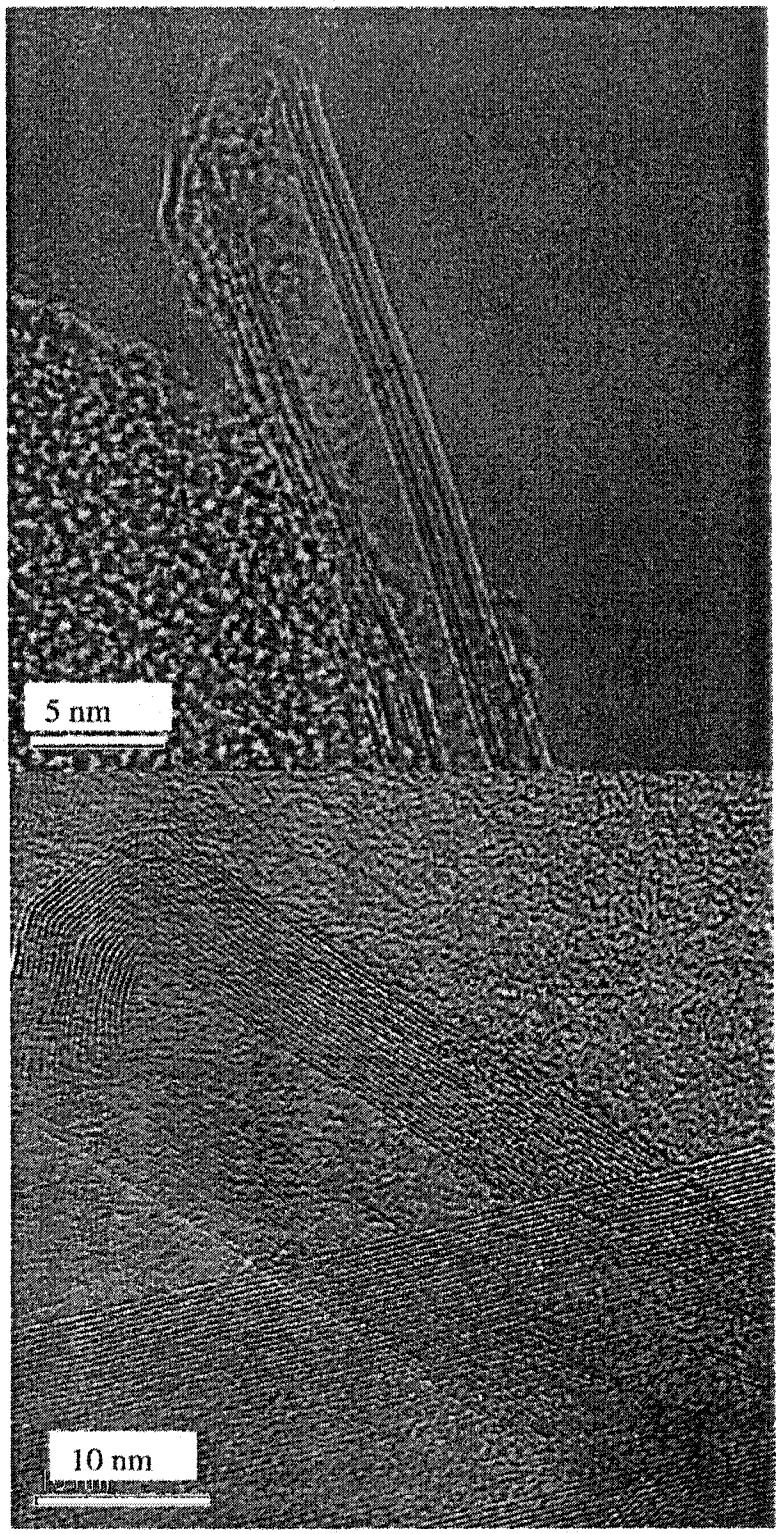

Figure 33: HR-TEM Images of NASA Goddard Space Flight Center Multi-wall CNTs Showing Distinct Wall Layers

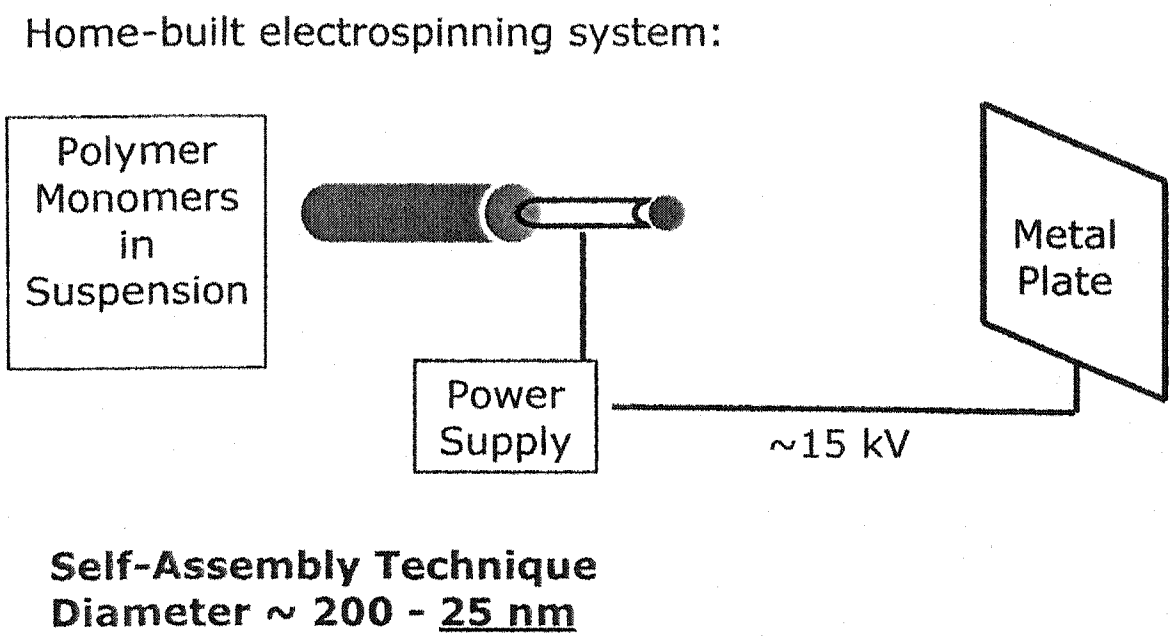

Figure 34: Electrospinning Set-up

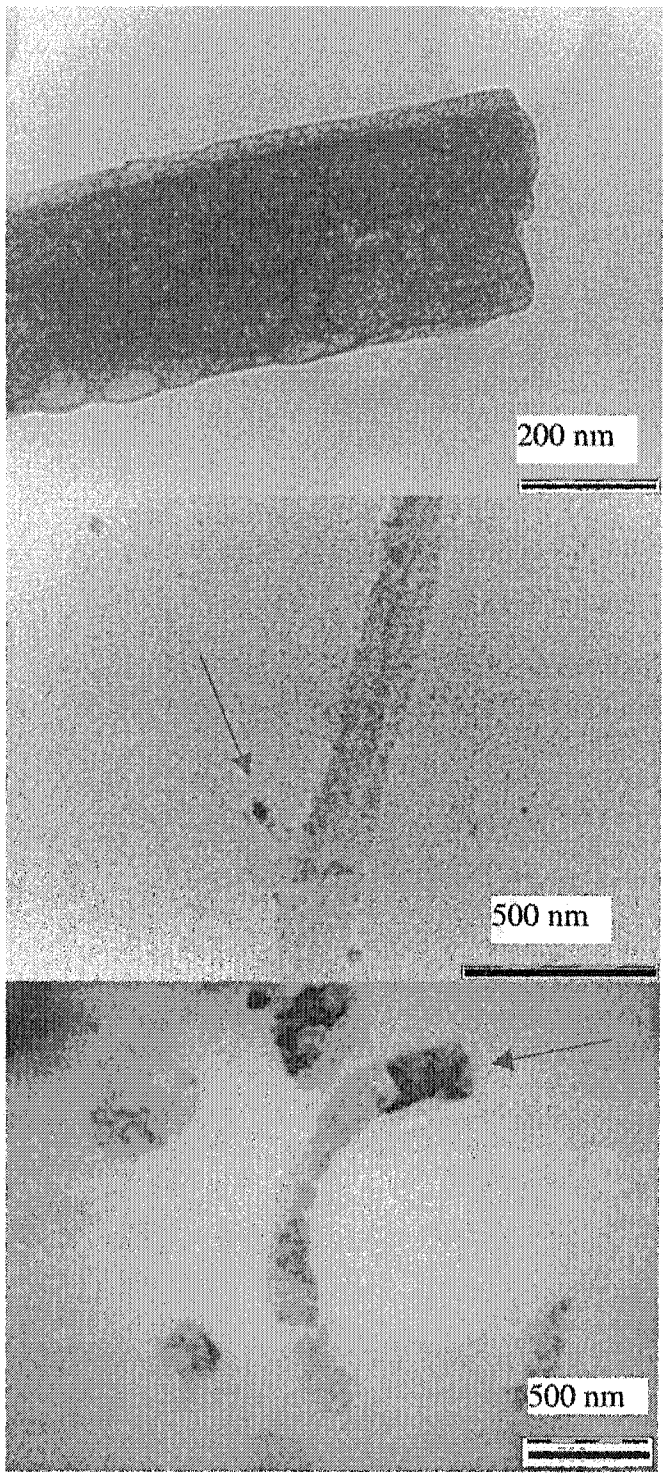

Figure 35: HR-TEM Images of Electrospun Carbon Nanofibers Showing Progressive Damage from 0- 900 seconds (a) Pre-irradiation (b) 90 seconds (c) 900 seconds

CHAPTER 6

DISCUSSION

The CNTs from the NASA Goddard Space Flight Center were not affected up to the highest radiation dose over 900 sec. These CNTs were shown by HRTEM and Raman to be high quality multi-wall CNTs with diameters ranging from 5-10 nm. They were produced via the carbon arc discharge method in a helium atmosphere at the NASA Goddard Space Flight Center. Single-wall CNTs from Carbon Nanotechnologies (Tubes@Rice) were also not affected up to the highest radiation dose over 900 sec. By contrast, two other hollow core carbon structures/nanostructures, vapor grown carbon fibers (VGCF) and electrospun carbon nanofibers (ESCNF), showed considerable damage by the highest radiation dose and significant damage even at the lower doses. The radiation damage mechanism appeared to be different for the VGCF and ESCNF, being possibly amorphitization in one case and local melting in the other. Thus, while these two different damage mechanisms were possible outcomes of our radiation experiments, neither seemed to apply to single and multi wall carbon nanotubes up to the radiation doses studied. These results indicate that CNT textiles and components may have good heavy ion radiation resilience that would make them appropriate for deployment in space applications.

Heavy ion radiation, although a significant component and a serious problem for low earth high declination orbits, is not the only type of radiation found in space. For example, another important feature in LEO is the South Atlantic Anomaly (SAA), which is an area of exceptionally high proton density, and placed over much of South America

and the South Atlantic Ocean. Currently those satellites that travel through the SAA experience higher rates of single event effects (SEE) than those that do not. In laboratory experiments on earth, it has been noted that purified single-wall CNTs (particularly isolated single-wall CNTs) do not appear to be stable under the electron beam of the electron microscope [63-64]. Multi-wall CNTs were also reported by Bursill *et al* to be unstable under the electron beam of the transmission electron microscope [64]. Electron radiation (gamma radiation) is also a type of ionizing radiation found in space. These reports underscore the need for total ionizing dose (TID) experiments on nanotube components and circuits. Our group currently has research efforts underway for TID experiments on nanotube components and nanotube circuits as part of a collaborative effort of Michigan State University with both the NASA Goddard Space Flight Center and the NASA Jet Propulsion Laboratory.

Transport

Transport studies are the major emphasis of the thesis project of Benjamin W. Jacobs, who will be continuing this research. Heavy-ion radiation and total dose effects on CNT and Gallium Nitride (GaN) nanowire-based nanocircuits will both be examined. Transport evaluation studies will be conducted with scanning tunneling microscopy, two-point, and four-point probe measurements. Some of these studies will also investigate the effect of thermal variation on transport, using the world-class cryogenic facilities at the NASA Goddard Space Flight Center (micro to milli Kelvin).

Gold and Palladium contacts will both be investigated. The goals of this part of the research are to carefully investigate the nature of the Schottky-barrier at the nanocontacts.

NASA has a well-established generic need for radiation tolerant technologies for flight electronics, spanning from spacecraft systems to scientific instruments. Current state-of-the-art radiation-hard microelectronics cannot be used without heavy shielding in environments such as the Jovian or in proximity of a Radioisotope Thermal Generator (RTG). This impacts heavily the mass budget of a mission. A potential solution to this problem can be sought in using nanometer-sized devices, whose small active volume makes them inherently radiation tolerant. During the transport studies, the electrical characteristics will be monitored for changes as a function of the absorbed dose. The results will be analyzed to (1) extract the essential characteristics of the technology, (2) evaluate its radiation tolerance, and (3) assess the feasibility of nanotechnology for infusion in NASA missions.

APPENDIX A

Preparation Procedure for TEM Grids With Holey Carbon Film

1 Dissolve about 0.4% formvar or butvar in chloroform (make about 100ml), add about 1% glycerol and shake until you have an emulsion.

2. Decant into a tall 25 ml beaker and dunk a clean glass slide into the solution. Remove from the solution at a slow but constant rate. Allow it to flash in a vertical position.

3. Hold the dried slide in a saturated steam plume until its well beaded with condensate but the condensate isn't sheeting.

4 Scrape the edges of the slide with a plastic bottle cap to break the film free.

5 Float the film off the slide by gently immersing the slide in a dish of DI water. It should appear to silver to gray in reflected light.

6 Make an array of grids on the film.

7 Lay a piece of paper (typing paper or a PostIt note paper) over the grids and allow the paper to wet.

8. Gently lift the paper off the water surface and allow to dry, grid side up.

9. When dry, carbon coat.

10. Place the carbon coated grids, still on the lifting paper in a glass petri dish into which you've placed a pad of filter paper completely soaked in chloroform. Cover and allow the petri dish to stand under a hood until the chloroform flashes off.

APPENDIX B

Irradiation Procedure using the Coupled Cyclotron Facility at the National Superconducting Cyclotron Laboratory

Samples were irradiated using a primary beam of ^{86}Kr at 142A MeV. When having 142 MeV per nucleon, ^{86}Kr has a total energy of 12.212 GeV. The beam was transported to the NSCL's N4 vault end station by dipole and quadrupole magnets, and focused there to an area having dimensions of 2-cm (height) by 2-cm (width), as measured from known dimensional markings on the beam-viewing scintillator placed at the beam line exit vacuum window. The vacuum window was a zirconium foil, having a diameter of about 7 cm and a thickness of about 0.02159 mm.

The beam current was initially measured at the exit point using a Faraday cup. A beam stop was pressed into a long copper pipe for accurate electron current collection. The beam stop was a solid cylinder of Hevimet[a], an alloy of tungsten, nickel, and copper. Its diameter was 5.08 cm and its length was 5.093 cm. Insulating rings were placed around the Hevimet-copper-pipe assembly, and the assembly was placed in the beam line, forming a Faraday cup for current integration. For reference, the range[b] in Hevimet of an ion of ^{86}Kr having 12,212 MeV is about 1.12 mm.

The upstream current was measured in the extraction channel of the K1200 cyclotron, using a remotely operated beam probe. The exit and upstream current measurements were ratioed to assess a beam transmission factor. For each subsequent experiment, the upstream current was measured both before and after the run. From this,

a stable current of 0.3 particle-picoamperes (ppA) was estimated as the beam current at the exit point during the experiments.

a HD18, by Mi-Tech Metals, Inc., 1340 N. Senate Ave., Indianapolis, IN 46202; HD18 is 95% tungsten, 3.5% Ni, and 1.5% copper, and has a density of 18 g/cm^3.
[b] Ranges and energy losses reported in our paper were calculated using the computer code SRIM-2003: J. F. Ziegler and J. P. Biersack, SRIM code, http://www.srim.org/ (2003).

BIBILIOGRAPHY

[1] N. Bingefors, T. Ekelöf, C. Eriksson, G. Mörk, M. Paulsson, and A Sjölund, "Radiation Hardness Tests with a Demonstrator Preamplifier Circuit Manufactured in Silicon on Sapphire (SOS) VLSI Technology", Nuclear Instruments and Methods A, Vol. 316 (2-3) pp. 349-363 (1992)

[2] S. J. Mathew, G. Niu, S.D. Clark, J.D. Cressler, M.J. Palmer, and W.B. Dubbelday, "Radiation-Induced Back-channel Leakage in SiGe CMOS on Silicon-on-Sapphire (SOS) Technology", IEEE Transactions on Nuclear Science, Vol. 46 (6) pp. 1848-1853 (1999)

[3] C.F. Edwards, W. Redman-White, M. Bracey, B.M. Tenbroek, M.S.L. Lee and M.J. Uren, "A Multibit ΣΔ Modulator in Floating-Body SOS/SOI CMOS for Extreme Radiation Environments", IEEE Journal of Solid-State Circuits, Vol. 34 (7) pp. 937-948 (1999)

[4] K.P.H. Lui and F.A. Hegmann, "Ultrafast Carrier Relaxation in Radiation-Damaged Silicon on Sapphire Studied by Optical-Pump-Terahertz-Probe Experiments", Applied Physics Letters, Vol. 78 (22) pp. 3478-3480 (2001)

[5] J. Handon and H. Veloric, "Radiation Hardened Silicon-on-Sapphire", Electronic Engineering, Vol. 56 (685) pp. 61-62 (1984)

[6] F.Z. Cui, Z.J. Chen, J. Ma, G.R. Xia and Y. Zhai, "Atomistic Simulation of Radiation Damage to Carbon Nanotube", Physics Letters A, Vol. 295, pp. 55-59 (2002)

[7] V.V. Klimov and V.S. Letokhov, "Hard X-radiation Emitted by a Positron Moving in a Carbon Nanotube", Physica Scripta, 56 (5) pp. 480-486 (1997)

[8] S. Iijima, "Helical Microtubules of Graphitic Carbon", Nature, Vol. 354, pp. 56-59 (1991)

[9] R.O. Avakian, L.A. Gevorgian, K.A. Ispirian and R.K. Ispirian, "Spontaneous and Stimulated Radiation of Particles in Crystalline and Nanotube Undulators", Nuclear Instruments and Methods B, Vol. 173, pp. 112-120 (2001)

[10]V.V. Klimov, and V.S. Letokhov, "Hard-directional X-radiation Emitted by a Charged Particle Moving in a Carbon Nanotube", Physics Letters A, Vol. 222, (6) pp. 422-428 (1996)

[11] V.V. Klimov and V.S. Letokhov, "Monochromatic Gamma-radiation Emitted by a Relativistic Electron Moving in a Carbon Nanotube", Physics Letters A, Vol. 226 (3-4) pp. 244-252 (1997)

[12] D. Grimm, R.B. Muniz, and A. Latgé, "From Straight Carbon Nanotubes to Y-shaped Junctions and Rings", Physical Review B, Vol. 68 (19) pp. 193407-19310 (2003)

[13] R. Saito, G. Dresselhaus, and M. Dresselhaus, *Physical Properties of Carbon Nanotubes*, by Imperial College Press, London (1998)

[14] S.J. Tans, A.R.M. Verschueren, and C. Dekker, "Room-temperature Transistor Based on a Single Carbon Nanotube", Nature, Vol. 393, pp. 49-52 (1998)

[15] M.M. J. Treacy, T.W. Ebbesen, and J.M. Gibson, "Exceptionally High Young's Modulus Observed for Individual Carbon Nanotubes", Nature, Vol. 381, pp. 678-680 (1996)

[16] A.T. Woolley, C. Guillemette, C.L. Cheung, D.E. Housman and C.L. Lieber, Nature Biotechnology, "Direct Haplotyping of Kilobase-Size DNA Using Carbon Nanotube Probes", Vol. 18 pp. 760-779 (2000)

[17] J. Cumings and A. Zettl, "Low Friction Nanoscale Linear Bearing Realized From Multiwall Carbon Nanotubes", Science, Vol. 289, pp. 602-604 (2000)

[18] B.C. Edwards, "Design and Deployment of a Space Elevator", Acta Astonautica, Vol. 47 (10) pp. 735-744 (2000)

[19] Q. Wang and J.K. Johnson, "Optimization of Carbon Nanotube Arrays for Hydrogen Adsorption", Journal of Physical Chemistry B, Vol. 103, pp. 4809-4813 (1999)

[20] X. Qin, X.P. Gao, H.Liu, H.T. Yuan, D.Y. Yan, W.L. Gong, and D.Y. Song, "Electrochemical Hydrogen Storage of Multi-Wall Carbon Nanotubes", Electrochemical and Solid-State Letters, Vol. 3 (12) pp. 532-535 (2000)

[21] A.G. Rinzler, J.H. Hafner, P. Nikolaev, L. Lou, S.G. Kim, D. Tomanek, P. Nordlander, D.T. Colbert, and R.E. Smalley, "Unraveling Nanotubes: Field Emission From an Atomic Wire", Science, Vol. 269 (5230) pp. 1550-1553 (1995)

[22] W.A. de Heer, A. Chatelain, and D. Ugarte, "A Carbon Nanotube Field Emission Electron Source", Science Vol. 270 (5239) pp. 1179-1180 (1995)

[23] P.G. Collins and A. Zettl, "A Simple and Robust Electron Beam Source From Carbon Nanotubes", Applied Physics Letters, Vol. 69 (13) pp. 1969-1971 (1996)

[24] Y. Cheng Y and O. Zhou, "Electron field emission from carbon nanotubes", Comptes Rendus Physique, Vol. 4, pp. 1021-1033 (2003); O. Zhou, S. Chang, Y. Cheng Y and J. Zhang, "Potential applications of nanotechnology in radiation oncology", Medical Physics, Vol. 30, pp. 1414-1414 (2003)

[25] S. Iijima, "Growth of Carbon Nanotubes", Materials Science and Engineering, Vol. B19, pp. 172-180 (1993)

[26] B.W. Smith, M. Monthioux, and D.E. Luzzi, "Carbon Nanotube Encapsulated Fullerenes: A Unique Class of Hybrid Materials", Chemical Physics Letters, Vol. 315, pp. 31-36 (1999)

[27] C.-H. Kiang and W.A. Goddard III, "Polyyne Ring Nucleus Growth Model for Single-Layer Carbon Nanotubes", Physical Review Letters, Vol. 76 (14) pp. 2515-2518 (1996)

[28] H. Kanzow and A. Ding, "Formation Mechanism of Single-Wall Carbon Nanotubes on Liquid-Metal Particles", Physical Review B, Vol. 60 (15) pp. 11180-11186 (1999)

[29] C-H. Kiang , W.A. Goddard III, R. Beyers and D.S. Bethune, "Carbon Nanotubes With Single-Layer Walls", Carbon Vol. 33 (7) pp. 903-914 (1995)

[30] J. Mossbrucker, "Measurement and Characterization of the Raman Spectrum of Diamond Films", M.S. Thesis, Michigan State University (1994)

[31] M.I. Stockman, V.M. Shalaev, M. Moskovits, R. Botet, and T.F. George, "Enhanced Raman scattering by fractal clusters: Scale-invariant theory" Physical Review B, Vol. 46, pp. 2821-2830

[32] C. Qin and L. –M. Peng, "Measurement Accuracy of the Diameter of a Carbon Nanotube from TEM Images", Physical Review B, Vol. 65, pp. 155341 (2002)

[33] A.A. Lucas, V. Bruyninckx, and P. Lambin, "Calculating the Diffraction of Electrons or X-rays by Carbon Nanotubes", Europhysics Letters, Vol. 35 (5) pp. 355-360 (1996)

[34] A.G. Rinzler, J. Liu, H. Dai, P. Nikolaev, C.B. Huffman, F.J. Macias-Rodriguez, P.J. Boul, A.H. Lu, D. Heymann, D.T. Colbert, R.S. Lee, J.E. Fisher, A.M. Rao, P.C. Eklund and R.E. Smalley, "Large-Scale Purification of Single-Wall Carbon Nanotubes: Process, Product, and Characterization", Applied Physics A, Vol. 67, pp. 29-37 (1998)

[35] M.S. Gudiksen, L.J. Lauhon, J. Wang, D.C. Smith, and C.M. Lieber, "Growth of Nanowire Superlattice Structures for Nanoscale Photonics and Electronics", Nature, Vol. 415, pp.617-620 (2002)

[36] C.M. Lieber, "Nanowire Superlattices", Nano Letters, Vol. 2, pp. 81-82 (2002)

[37] J. Hu, M. Ouyang, P. Yang, and C. M. Lieber, "Controlled Growth and Electrical Properties of Heterojunctions of Carbon Nanotubes and Silicon Nanowires", Nature, Vol. 399, pp. 48-51 (1999)

[38] Y. Wu, R. Fen, and P. Yang, "Block-by-Block Growth of Single-Crystalline Si/SiGe Superlattice Nanowires", Nano Letters, Vol. 2, pp. 83-86 (2002)

[39] M.T. Bjork, B.J. Ohlsson, T. Sass, A.I. Persson, C. Thelander, M.H. Magnusson, K. Deppert, L.R. Wallenberg, and L. Samuelson, "One-Dimensional Heterostructures in Semiconductor Nanowhiskers", Applied Physics Letters, Vol. 80, pp. 1058-1060 (2002)

[40] M.T. Bjork, B.J. Ohlsson, T. Sass, A.I. Persson, C. Thelander, M.H. Magnusson, K. Deppert, L.R. Wallenberg, and L. Samuelson, "One-Dimensional Steeplechase for Electrons Realized", Nano Letters, Vol. 2, pp. 87-89 (2002)

[41] Y.F. Zhang, Y.H. Tang, Y. Zhang, C.S. Lee, I. Bello, and S.T. Lee, "Deposition of Carbon Nanotubes on Si Nanowires by Chemical Vapor Deposition", Chemical Physics Letters, Vol. 330, pp. 48-52 (2000)

[42] G. A. Hebner, "Spatially resolved Excited State Densities and Neutral and Ion Temperatures in Inductively Coupled Argon Plasmas", Journal of Applied Physics, Vol. 80, pp. 2624-2636 (1996)

[43] P. Hargis Jr., K. Greenberg, P. Miller, J. Gerado, J. Torczynski, M. Riley, G. Hebner, J. Roberts, J. Olthoff, J. Whetstone, R. Van Brunt, M. Sobelewski, H. Anderson, M. Splichal, J. Mock, P. Bletzinger, A. Butterbaugh, M. Brake, M. Passow, J. Pender, A. Lujan, M. Elta, D. Graves, H. Sawin, M. Kushner, J. Verdeyen, R. Horwath, and T. Turner, "The GEC Reference Cell: A Defined Parallel-Plate RF-System for Experimental and Theoretical Studies of Plasma Processing Discharges", Review of Scientific Instruments, Vol. 65, pp. 140-154 (1994)

[44] C.J. Collard, "Growth of CNT in an Inductively Coupled Plasma", Chapter 4, Ph.D. Thesis, University of Michigan (2002)

[45] B. Qi, R.M. Gilgenbach, Y.Y. Lau, M.D. Johnston, J. Lian, L.M. Wang, G.L. Doll, and A. Lazarides, "Ablation Plasma Ion Implantation Experiments: Measurement of Fe Implantation Into Si", Applied Physics Letters, 78 pp. 3785-3787 (2001)

[46] B. Qi, Y.Y. Lau, and R.M. Gilgenbach, "Extraction of Ions From the Matrix Sheath in Ablation-Plasma Ion Implantation", Applied Physics Letters, 78 pp. 706-708 (2001)

[47] B. Sundaray, V. Subramanian, T.S. Natarajan, R.-Z. Xiang, C.-C. Chang, and W-S. Fann, "Electrospinning of continuous aligned polymer fibers", Applied Phys. Letters, Vol. 84, pp.1222-1224 (2004)

[48] G. Tibbetts, "Applications Research on Vapor Grown Carbon Fibers", *Science and Application of Nanotubes*, pp. 35-51, , Eds. D. Tomanek and R. Enbody, Kluwer Academic Press, 2000, New York

[49] P. Corio, S.D.M. Brown, A. Marucci, M.A. Pimenta, K. Kneipp, G. Dresselhaus, and M.S. Dresselhaus, "Surface-Enhanced Resonant Raman Spectroscopy of Single-Wall Carbon Nanotubes Adsorbed on Silver and Gold Surfaces", Physical Review B, Vol. 61, pp. 13202-13211 (2000)

[50] L. C. Qin, T. Ichihashi and S. Iijima, "On the Helicity of Carbon Nanotubes", Ultramicroscopy, Vol. 67, pp. 181-189 (1996)

[51] G.S. Oerhlein, J.F. Rembetski and E.H. Payne, "Study of Sidewall Passivation and Microscopic Silicon Roughness Phenomena in Chlorine-based Reactive Ion Etching of Silicon Trenches", Journal of Vacuum Science and Technology B, Vol. 8, pp.1199-1211 (1990)

[52] E.I. Givargizov, A.N. Stepanova, L.N. Obolenskaya, E.S. Mashkova, V.A. Molchanov, M.E. Givargizov, and I.W. Rangelow, "Whisker Probes", Ultramicroscopy, Vol.. 82, pp. 57-61 (2000)

[53] P.S. Nam, L.M. Ferreira, T.Y. Lee, and K.N. Tu, "Study of Grass Formation in GaAs Backside Via Etching Using Inductively Coupled Plasma System", Journal of Vacuum Science and Technology B, Vol. 18, pp. 2780-2784 (2000)

[54] J.E. Parmeter, R.J. Shul, A.J. Howard, and P.A. Miller, "Treatment of InP Surfaces in Radio Frequency H-2 and H-2/CH4/Ar Plasmas: In Situ Compositional Analysis, Etch Rates, and Surface Roughness", Journal of Vacuum Science and Technology B, Vol. 14, pp. 3563-3574 (1996)

[55] N.J. Pinto, A.T Johnson, A.G. MacDiarmid, C.H. Mueller, N. Theofylaktos, D.C. Robinson, and F.A. Miranda, "Electrospun Polyaniline/Polyethylene Oxide Nanofiber Field-Effect Transistor", Applied Physics Letters, Vol. 83 (20) pp. 4244-4246 (2003)

[56] J.P. Bibring and F. Rocard, "Ion-Implantation Phenomena in Space", Radiation Effects and Defects in Solids, Vol. 65 (1-4) pp. 159-165 (1982); M. Maurette, "Ion-Implantation Effects in Space", Nuclear Instruments and Methods, Vol. 132, pp. 579-586 (1976)

[57] C. Ruehlicke, MA Briere, and D. Schneider, "AFM Studies of a New Type of Radiation Defect on Mica Surfaces, Caused by Highly-Charge Ion Impact", Nuclear Instruments and Methods in Physics Research B, Vol. 99 (1-4) 528-531 (1995)

[58] C. Ascheron, J.P. Biersack, P. Goppeltlanger, and J. Erxmeyer, "Influence of Ionization Processes on Radiation Defect Formation", Nuclear Instruments and Materials in Physics Research B, Vol. 80 (1) pp. 3-6 (1993)

[59] "Handbook of Accelerator Physics and Engineering", edited by Alexander Wu Chao and Maury Tigner, World Scientific, River Edge, NJ (1999)

[60] Schindler group, Department of Biochemistry and Molecular Biology

[61] D.M. Fleetwood, P.S. Winokur, and P.E. Dodd, "An Overview of Radiation Effects on Electronics in the Telecommunications Environment", Microelectronics Reliability Vol. 40, pp. 17-26 (2000)

[62] Z.L. Wang, P. Poncharal, and W.A. de Heer, "Nanomeasurements of Individual Carbon Nanotubes by In Situ TEM", Pure and Applied Chemistry, Vol. 72 (1-2) pp. 209-219 (2000)

[63] Z.L. Wang, P. Poncharal, W.A. de Heer, Z.R. Dai, and Z.W. Pan, "Mechanical and Electrostatic Properties of Carbon Nanotubes and Nanowires", Materials Science and Engineering C, Vol. 16 (1-2) pp. 3-10 (2001)

[64] LA. Bursill, J.-L. Peng, and X.-D. Fan, "Cross-Sectional High-Resolution Transmission Electron Microscopy Study of the Structures of Carbon Nanotubes", Philosophical Magazine A, Vol. 71 (5) pp. 1161-1176 (1995)

[65] D.A. Evans and M.A. Crook, "Irradiation of Plastics: Damage and Gas Evolution", MRS Bulletin Special Issue: Materials Performance in a Radiation Environment, Vol. 22, pp. 36-41 (1997)

[66] T.D. Burchell, "Radiation Effects in Graphite and Carbon-Based Materials", MRS Bulletin Special Issue: Materials Performance in a Radiation Environment, Vol. 22, pp. 29-35 (1997)